Thermal Evolution of an Active Region Through Quiet and Flaring Phases as Observed by NuSTAR, XRT, and AIA

Jessie Duncan[1,7] , Reed B. Masek[2] , Albert Y. Shih[1] , Lindsay Glesener[2] , Will Barnes[1,3] , Katharine K. Reeves[4] ,
Yixian Zhang[2] , Iain G. Hannah[5] , and Brian W. Grefenstette[6]
[1] NASA Goddard Space Flight Center, Greenbelt, MD, USA
[2] University of Minnesota, Minneapolis, MN, USA
[3] American University, Washington, DC, USA
[4] Harvard-Smithsonian Center for Astrophysics, Cambridge, MA, USA
[5] University of Glasgow, Glasgow, UK
[6] California Institute of Technology, Pasadena, CA, USA

Abstract

Solar active regions (ARs) contain a broad range of temperatures, with the thermal plasma distribution often observed to peak in the few millions of kelvin. Differential emission measure (DEM) analysis can allow instruments with diverse temperature responses to be used in concert to estimate this distribution. Nuclear Spectroscopic Telescope ARray (NuSTAR) hard X-ray (HXR) observations are uniquely sensitive to the highest-temperature components of the corona, and thus extremely powerful for examining signatures of reconnection-driven heating. Here, we use NuSTAR diagnostics in combination with extreme-ultraviolet and soft X-ray observations (from the Solar Dynamics Observatory/Atmospheric Imaging Assembly and Hinode/X-Ray Telescope) to construct DEMs over 170 distinct time intervals during a 5 hr observation of an alternately flaring and quiet active region (NOAA designation AR 12712). This represents the first HXR study to examine the time evolution of the distribution of thermal plasma in an AR. During microflares, we find that the initial microflare-associated plasma heating is predominantly heating of material that is already relatively hot, followed later on by broader heating of initially cooler material. During quiescent times, we show that the amount of extremely hot (>10 MK) material in this region is significantly (∼2–4 orders of magnitude) less than that found in the quiescent AR observed in HXRs by FOXSI-2. This result implies there can be radically different high-temperature thermal distributions in different ARs, and strongly motivates future HXR DEM studies covering a large number of these regions.

Unified Astronomy Thesaurus concepts: The Sun (1693); Solar physics (1476); Solar x-ray emission (1536); X-ray telescopes (1825); Solar extreme ultraviolet emission (1493); Solar active regions (1974); Solar corona (1483); Solar coronal heating (1989)

1. Introduction

Plasma in the solar corona is persistently observed to be much hotter than the ∼6000 K photosphere, with active regions (ARs) typically found to be at temperatures of 2–3 MK or greater. The source of energy leading to this elevated temperature must be the solar magnetic field. It is so far unclear which mechanism is dominant in converting magnetic energy into consistent coronal heating.

During solar flares, energy is released through magnetic reconnection, as coronal magnetic fields abruptly relax to a lower-potential state. Significant heating of AR plasma occurs in flares. However, observed solar flares occur insufficiently often to explain the persistently elevated temperature of the corona as a whole (e.g., Shimizu 1995).

Reconnection still may lead to coronal heating instead, via a large ensemble of "nanoflares," tiny events too faint to individually observe (Parker 1988). It is unknown exactly how released magnetic energy would be converted to plasma

heating in these events; one method for investigating this mechanism is the continued study of energy release and plasma heating in microflares, the smallest flares we *can* individually observe (e.g., Christe et al. 2008; Hannah et al. 2008; Athiray et al. 2020; Cooper et al. 2021). One consistent property is that the hottest flare-heated plasma is present early in the evolution of the event, more closely linked to the initial energy release.

Nanoflare (or low-frequency coronal) heating can be contrasted with theories of heating via magnetohydrodynamic wave dissipation, which involve a continuous input of energy into the corona (high-frequency heating; Van Doorsselaere et al. 2020). An unambiguous observational signature of low-frequency heating is the presence of faint, extremely hot plasma (>7 MK) occurring in the absence of any observable impulsive event (Cargill 1994; Cargill & Klimchuk 2004).

To characterize plasma heating at quiet *or* flaring times, it is desirable to determine the distribution of thermal plasma present as a function of time, particularly the highest-temperature material. Differential emission measure (DEM) analysis allows estimation of the emission measure distribution (EMD) of a source as a function of temperature, starting from observation(s) of a source and the temperature response(s) of the observing instrument(s).

There have been a wealth of quiescent AR DEM studies (summarized, for example, in Barnes et al. 2016a) utilizing

---

[7] NASA Postdoctoral Program.

extreme-ultraviolet (EUV) and soft X-ray (SXR) diagnostics from Hinode's EUV Imaging Spectrometer (EIS) and X-Ray Telescope (XRT), as well as the Atmospheric Imaging Assembly (AIA) aboard the Solar Dynamics Observatory (SDO; Culhane et al. 2007; Golub et al. 2007; Lemen et al. 2012). However, the combination of these instruments is insufficiently sensitive to faint components above 5 MK (Winebarger et al. 2012). Additionally, especially short-lived hot plasma may not produce signatures in the hot EUV spectral lines observed by EIS and AIA, due to a lack of ionization equilibrium (e.g., Bradshaw & Mason 2003; Bradshaw & Klimchuk 2011).

A powerful alternate diagnostic for constraining high-temperature material is the thermal bremsstrahlung continuum as observed in the hard X-ray (HXR) range (e.g., Ishikawa & Krucker 2019). Only the high-energy tail of the electron distribution generates bremsstrahlung at HXR energies, biasing this diagnostic toward the hottest material. Additionally, continuum observations are much less sensitive to none-quilibrium ionization effects.

The Reuven Ramaty High Energy Solar Spectroscopic Imager (RHESSI) was a flare-optimized HXR indirect-imaging spectrometer. RHESSI's indirect-imaging method gave it limited sensitivity, due to a high nonsolar background. However, RHESSI was still useful for constraining or identifying high-temperature material. Considering quiescent times, Schmelz et al. (2009) used RHESSI to significantly constrain the hot plasma possible in a quiescent AR, when compared to results with EUV/SXR instruments alone. Additionally, RHESSI estimates of the plasma emission measure have identified the presence of a component above 5 MK at nonflaring times (McTiernan 2009; Reale et al. 2009). Finally, RHESSI can be incorporated in DEM analyses: Ishikawa & Krucker (2019) used RHESSI, XRT, and AIA to derive the DEM of a quiet AR, unambiguously identifying a faint >5 MK component. Unlike the majority of quiescent ARs, this region was bright enough in HXRs to be imaged by RHESSI (albeit via a long integration), likely indicating it was also hotter than the typical AR. That only particularly bright regions can be analyzed this way by RHESSI represents an observational bias.

Considering small transients, a large two-part RHESSI study examined flares from GOES A to C class, with the second paper utilizing RHESSI spectroscopy to extract isothermal approximations of the plasma heated in each (Christe et al. 2008; Hannah et al. 2008). Additionally, Inglis & Christe (2014) conducted a joint AIA-RHESSI analysis of 10 B-class microflares, in which forward-fitting of AIA data and RHESSI spectroscopy were combined to estimate parameters describing DEMs of an assumed functional form.

HXR telescopes which focus light directly onto a small detector plane can achieve significantly lower nonsolar background (higher sensitivity) than RHESSI, allowing for the identification of much fainter hot plasma sources. The Focusing Optics X-Ray Solar Imager (FOXSI) sounding rockets have pioneered the development of direct-focusing telescopes optimized for solar observation, with science observations available from three successful flights.[8] A quiescent AR observation made by FOXSI-1 significantly constrained the magnitude of a >8 MK component predicted by an EIS/XRT-only DEM of the region (Ishikawa et al. 2014). Additionally, nanoflare-associated hot plasma (>10 MK) was identified via

FOXSI-2/XRT DEM analysis of another quiescent AR observed for 30 s during the ~5 minute FOXSI-2 flight (Ishikawa et al. 2017). FOXSI-2 also observed microflares, DEMs of which are presented in Athiray et al. (2020). These results (achieved with only a few minutes of observation time during each flight) demonstrate the power of this type of instrument to increase our understanding of the highest-temperature components of ARs.

The Nuclear Spectroscopic Telescope ARray (NuSTAR) is an astrophysical focused HXR observatory, capable of solar observation with some operational caveats, discussed further in Section 3.2.3 (Harrison et al. 2013; Grefenstette et al. 2016). Direct focusing allows NuSTAR to achieve a nonsolar background more than 3 orders of magnitude lower than RHESSI (Grefenstette et al. 2016). However, NuSTAR has limited detector throughput, meaning it records only a fraction of incident emission when observing bright solar sources (low livetime; see Section 3.2.3). This limits our ability to utilize its tremendous sensitivity. Still, NuSTAR data has previously been used to place upper limits on the presence of hot plasma in one quiet AR (Hannah et al. 2016). The properties of that region were found to correspond well to predictions by hydrodynamic simulations of low-frequency nanoflare ensembles (Marsh et al. 2018). NuSTAR has also been used to study heating in two microflaring regions via DEM analysis (Wright et al. 2017; Cooper et al. 2020).

To summarize past use of HXR observations to explore AR plasma heating: RHESSI and FOXSI studies have found intermittent evidence for a faint hot component at quiescent times, suggesting low-frequency heating, with the clearest detection presented in Ishikawa et al. (2017) and confirmed via modeling in Marsh et al. (2018). NuSTAR has the capability to detect such a component, as well, but has not yet been used for DEM studies of quiescent ARs. On the microflare side, only four events have been subject to DEM analysis with HXRs: Wright et al. (2017) performed a DEM of the rise phase of an event; Cooper et al. (2020) performed preflare and flare-time DEMs; and Athiray et al. (2020) performed DEMs of portions of two microflares observed during the ~5 minute FOXSI-2 rocket flight. None of these have examined how the thermal distribution changes over the course of the flare.

In this work, we present a detailed thermal analysis of an AR observed by NuSTAR during an interval in which it both produced small microflares and also experienced times with no obvious transients. We perform DEMs utilizing NuSTAR, XRT (when available), and AIA for 170 distinct time intervals, allowing detailed inference into how the distribution of thermal plasma changes over time. This includes high-time-cadence DEM analysis of microflaring intervals.

We present this work as follows. In Section 2, we introduce the AR under study, and discuss prior literature regarding this region. Section 3 discusses the DEM process: considerations regarding data preparation for each instrument, time interval selection, and the DEM method itself. Section 4 summarizes and discusses results from the DEM analysis. Finally, Sections 5 and 6 provide further discussion and conclusions.

2. Overview of Active-region Observations

NOAA-designated AR 12712 was a bipolar region which produced two GOES C-class and >40 GOES B-class flares while transiting the solar disk. There was broad, multi-instrumental coverage of the region in the latter half of 2018 May 29,

---

[8] The fourth flight, FOXSI-4, is scheduled to occur in 2024.
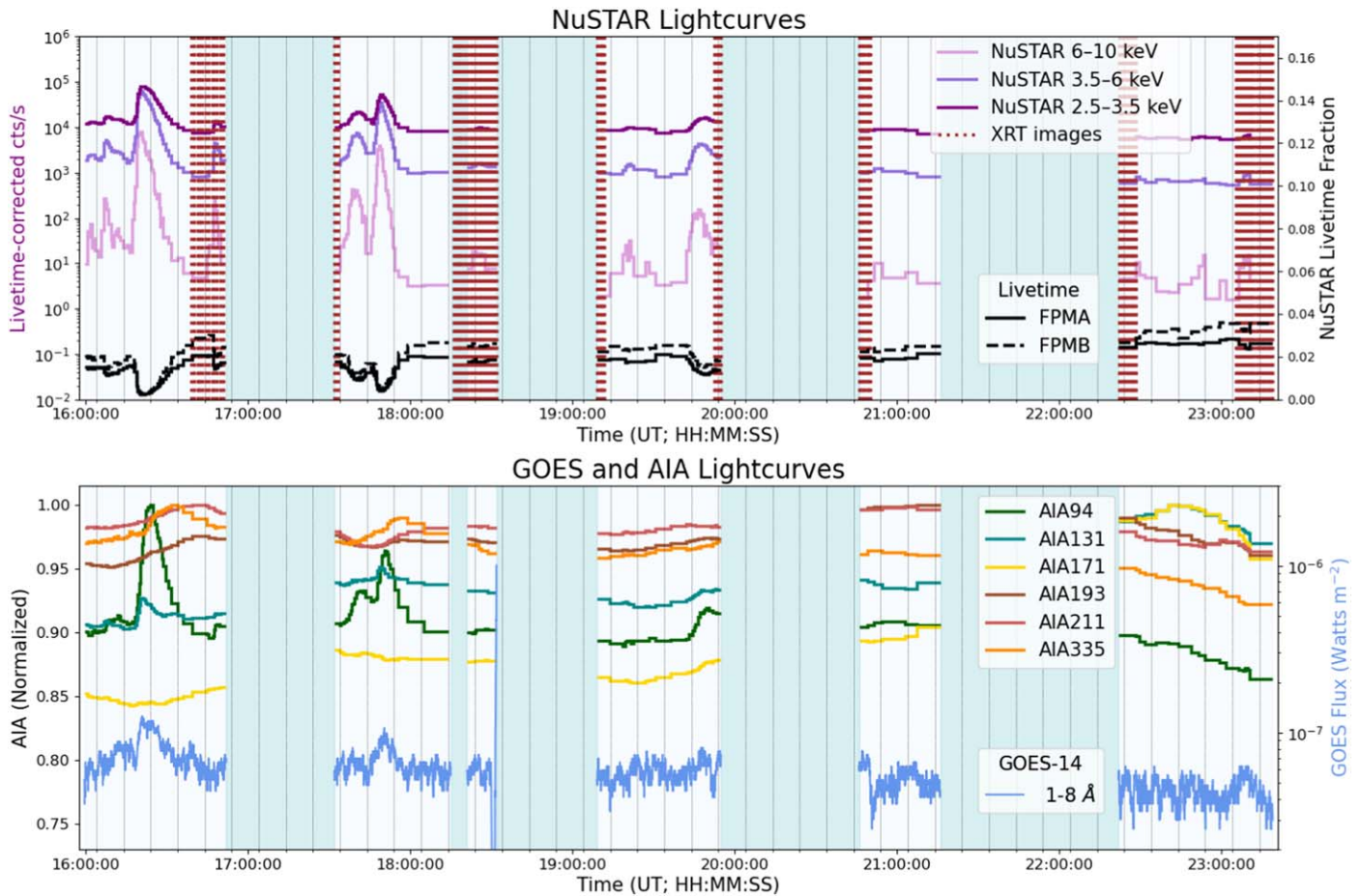
Figure 1. Time evolution of AR 12712 during the NuSTAR observation intervals. Time binning of lightcurves is according to the DEM time intervals (described in Section 3.3). Upper: the top three curves show NuSTAR livetime-corrected lightcurves in the three energy ranges used in DEM analysis; scale on left axis. NuSTAR livetime-corrected counts have been summed between its two telescopes (FPMA, FPMB; see Section 3.2.3). XRT observation times during the NuSTAR observations are marked. The lower two black curves show the livetime of each NuSTAR telescope during the same intervals; scale on right axis. Lower: on the left axis, AIA DEM inputs are shown for each DEM time interval; see Section 3.2.1 for details on data preparation. In this plot, the values in each AIA channel are normalized to their maximum over the entire duration of the observation. On the right axis, the GOES 1–8 Å flux is shown for the NuSTAR observation times.

motivated by the flight of the Hi-C 2.1 Sounding Rocket (Rachmeler et al. 2019). This included ∼5 hr of coverage by NuSTAR within a ∼7 hr period (15:55–23:20 UTC). As shown in Figure 1, the GOES flux during the NuSTAR observations primarily remained at the A level (defined as $<10^{-7}$ W m^{-2} in the 1–8 Å channel), briefly reaching B level during the largest microflare.

A previous NuSTAR study of this AR focused specifically on flaring times (Duncan et al. 2021), providing spectroscopy, time-profile analysis, and imaging of seven events ranging from GOES sub-A1 class up to B1 (see table of individual microflare GOES classes in Duncan et al. 2021). That study found no evidence for a nonthermal accelerated particle distribution as a source of the observed NuSTAR emission in any of the microflares. Because of this, the analysis presented here presumes that all NuSTAR-observed emission from the region has a thermal origin.

Hinode/EIS and XRT also observed this AR on 2018 May 29. While the EIS and NuSTAR observations overlap for just a few minutes, there are a number of intervals with joint NuSTAR/XRT coverage. The time profile of the AR over the entire observation interval is shown in Figure 1, which includes NuSTAR livetime-corrected lightcurves in several energy ranges, as well as marked times during the NuSTAR coverage

where XRT images are available. Figure 1 also shows the evolution of emission from the AR as observed by several AIA channels.

In conjunction with analysis of the Hi-C 2.1 results, Warren et al. (2020) performed a DEM analysis of the core of this AR using AIA, XRT, and EIS. The Hi-C 2.1 flight and interval covered by the Warren et al. (2020) DEM occurred during a NuSTAR nighttime. Discussion of the Warren et al. (2020) results in comparison with those of this study is included in Section 5.

3. Differential Emission Measure Analysis

In the following, we introduce the concept of DEM analysis and details of the DEM calculation itself (Section 3.1), the preparation of data and instrument responses for each instrument (Section 3.2), and the time intervals selected for analysis (Section 3.3).

3.1. DEM Calculation

In a situation where multiple instruments have observed emission from the same thermal plasma source, the measurements made by each observing instrument (M_i) can be

expressed as

$$M_i = \int R_i(T)\xi(T)dT, \qquad (1)$$

where $R_i(T)$ is the response of each instrument (i) as a function of temperature (T), and $\xi(T)$ is the line-of-sight DEM of the source as a function of T (in units of cm^{-5} K^{-1}). DEM calculation consists of inverting this expression in order to find $\xi(T)$, based on the M_i and R_i. The EMD as a function of temperature can also be extracted:

$$EMD = \xi(T)dT \qquad (2)$$

(in units of cm^{-5}). Figures in this work presenting DEM results all show the EMD distribution, as it is more straightforward to interpret with respect to results from HXR spectroscopy.

In this analysis, the DEM was computed using the regularized inversion method originally presented in Hannah & Kontar (2012) for use with data from instruments aboard Hinode and SDO (referenced henceforth as the "DEMREG" method). Specifically, this study makes use of the Python implementation of DEMREG, which has been previously used with data sets involving NuSTAR (e.g., Paterson et al. 2023). To estimate the uncertainty in each DEM solution, the DEM calculation was rerun iteratively (100×) while varying the inputs normally (with σ defined as the measurement uncertainty, described for each instrument in Section 3.2).

In addition to DEMREG, the standard Hinode/XRT Solar-Soft/SSWIDL procedure `xrt_dem_iterative2.pro` was used with the same input data and responses from all instruments in each DEM interval to generate alternative DEM solutions.[9] This method also uses an iterative procedure to determine uncertainty bounds on the output solution (here, iterated 1000×). The addition of this secondary method provides confirmation of certain physical conclusions.

The initial temperature range over which DEMs were computed was $\log(T) = 5.6$–7.2 (see Section 4.3.2 for more discussion of temperature bounds). In order to compare DEM results to the input data, the DEM is convolved with the instrument temperature responses to generate the DEM-predicted emission observed by each instrument. These residuals are shown in the lower-right-hand panels of all example figures, e.g., Figure 3. DEM residuals are discussed further in Section 4.3.2.

3.2. Data Preparation

3.2.1. Atmospheric Imaging Assembly

SDO/AIA provides continuous full-disk observation in a number of EUV passbands (Lemen et al. 2012). Here, AIA images in the 94, 131, 171, 193, 211, and 335 Å channels were used, as each have sensitivity to material at temperatures in the range associated with solar AR plasma. AIA channels are sensitive to multiple spectral lines with distinct peak formation temperatures; this leads to multiple peaks in each temperature response in Figure 2.

For each image in each channel, level 1 data were converted to level 1.5 with the use of the `calibrate` subpackage within the `aiapy` Python package. A correction was made for the

time-dependent degradation of the AIA instrument, also using `aiapy.calibrate`.

A spatial region was selected, encompassing the entire AR (a circular region, 150″ in radius). The rate of emission observed across this region within each AIA image was expressed in units DN s^{-1} pix^{-1}. For DEM time intervals of 30 s duration, we used the AIA image taken nearest to the midpoint of the interval. For DEM time intervals of >30 s duration (see Section 3.3 for discussion of time interval selection), the AIA per-pixel rate was averaged across the interval, with images selected at a 30 s cadence. Uncertainties in each AIA channel were found using the `estimate_error` function in `aiapy. calibrate`. A flat 10% uncertainty was added in quadrature to account for assumed uncertainty in the AIA responses, as was done in Zhang et al. (2023) to prepare AIA data for a joint DEM with RHESSI.

The AIA temperature response for each channel was acquired using the routine `aia_get_response.pro` (from the SSWIDL SDO/AIA library), using CHIANTI v9.3 coronal abundances (Dere et al. 1997, 2019). The `hissw` Python package was used to incorporate the functionality of these and other SSWIDL libraries while performing analysis in Python.

3.2.2. Hinode/XRT

Hinode/XRT uses multiple combinations of filters to make spatially resolved images of solar sources in the SXR band (Golub et al. 2007). XRT images of AR 12712 were available during only part of the NuSTAR interval, due to poor alignment between Hinode and NuSTAR daylight times during the observing campaign (see Figure 1). The XRT filter combinations used in this work were `Al_poly`, `Be_thin` and `Be_med`, each of which are sensitive to temperatures in the range between $\log(T) = 6.1$–7.5 (Golub et al. 2007); their response in our range of interest is shown in Figure 2. XRT images are taken at a range of exposure times, in order to image sources across a wide range in brightness (Golub et al. 2007). For the two thinner filters (`Al_poly`, `Be_thin`), we selected only images with exposure times in specific ranges, in order to exclude saturated images and brief, low-resolution "flare patrol" images (`Al_poly`, between 0.1 and 1 s; `Be_thin`, between 1 and 10 s).

For the selected images, the data were prepared by converting each image file from level 0 to level 1 using the `xrt_prep.pro` routine from the Hinode/XRT library within SolarSoft/SSWIDL. Pixel grade maps (an additional `xrt_prep.pro` output) were used to remove contamination spots (for Al_poly files only), as well as dust specks, hot pixels, and negative-value pixels for all files. After these steps, included pixels were selected using the same spatial regions as for AIA. To estimate uncertainties, ζ, in the individual pixel rates we used the expression

$$\zeta = (1 + \sqrt{DN + 0.75})/(\text{exposure time}), \qquad (3)$$

introduced to estimate XRT uncertainties for DEM analysis in Lee et al. (2017), where DN represents the individual pixel values (in units of DN). The total observed rate of XRT emission and uncertainty for each file (in units of DN s^{-1} pix^{-1}) were found by averaging the included pixel values and uncertainties. In the case where multiple suitable images were taken in the same XRT filter during the DEM time interval, the extracted pixel-averaged rates and uncertainties were averaged

---

[9] This was the method used in Ishikawa et al. (2014, 2017) and Ishikawa & Krucker (2019).
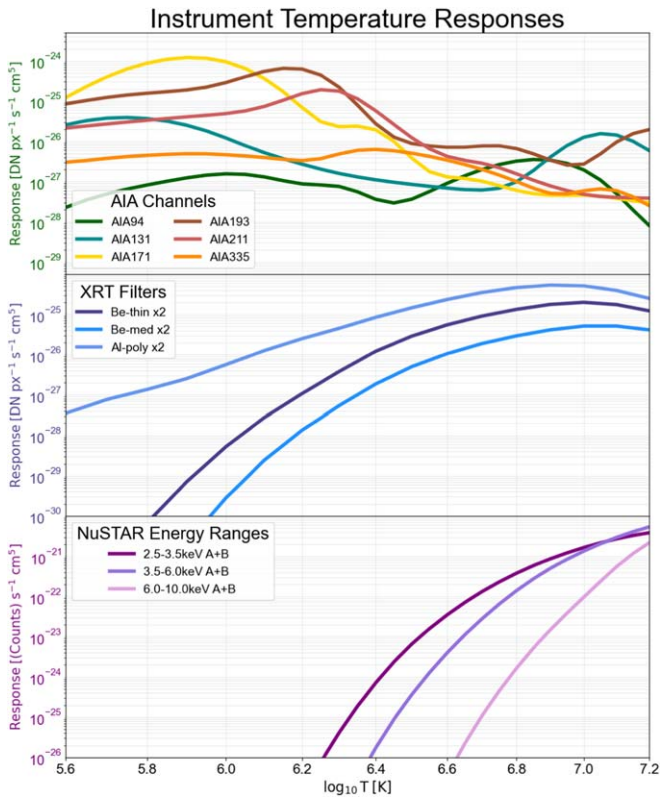
Figure 2. Temperature responses of instruments used in DEM analysis. Upper: AIA. Middle: XRT. Lower: NuSTAR.

over all suitable images as well. Finally, the output uncertainties from this process were added in quadrature with an additional 10% of the rate to account for uncertainty in the response.

The XRT temperature response for each filter combination was acquired using `make_xrt_temp_resp.pro` (also from the Hinode/XRT SSWIDL library). The default AIA emission model (with CHIANTI v9.3 coronal abundances; Dere et al. 1997, 2019) was used in the XRT response calculation, via the method described in the SolarSoft XRT Analysis Guide.[10] We multiply the XRT response functions by a factor of 2, a commonly employed correction factor discussed further in Appendix B.

3.2.3. NuSTAR

NuSTAR consists of two coaligned focusing X-ray telescopes, denoted hereafter by their focal plane modules, FPMA and -B (Harrison et al. 2013; Grefenstette et al. 2016). NuSTAR's telescopes have an angular resolution of 18″ FWHM, or 58″ HPD, significantly worse than the lower-energy instruments (AIA: 1″5; XRT: 2″). For the purposes of this analysis, we consider the entire AR as one source, as the NuSTAR resolution limits our ability to spatially isolate emission from the AR core.

Because NuSTAR is a spectrally resolved instrument, energy bin edges can be chosen to fit any scientific case at hand. Here, bins 2.5–3.5, 3.5–6, and 6–10 keV were chosen to sample a range of the temperatures to which NuSTAR is sensitive. The temperature responses of these energy ranges

are shown in Figure 2. The NuSTAR spatial region for each DEM interval was chosen by finding the center of mass of the NuSTAR emission during that interval, and selecting events recorded in a circular region 150″ in radius around that point.

The observed NuSTAR spectrum can be distorted by pileup. The effects of pileup are estimated by examining the relative incidence of different NuSTAR event "grades," particularly the "unphysical" grades that necessarily must involve more than one photon. In the time since the publication of Duncan et al. (2021), the NuSTAR heliophysics team has discovered that prior analysis methods underestimated the incidence of unphysical grade events, meaning that the pileup component of the NuSTAR spectra in that work was underestimated. Here, we find that a pileup correction *is* necessary, and subtract an estimate of the pileup component from the NuSTAR spectrum before incorporation into DEM analysis.[11] Because this correction leads to a preferential reduction in the higher-energy part of the NuSTAR spectrum, we remain confident in the conclusion from Duncan et al. (2021) that NuSTAR emission from the microflares observed in this AR has a solely thermal origin.

During observations of ARs and flaring activity, the limited rate capability of NuSTAR's detectors means the percent of time the detectors spend processing events begins to dominate over the percent of time the instrument is ready to register a new photon (livetime; Grefenstette et al. 2016). NuSTAR livetime ranged from 0.2% to 4% during this observation, which corresponds to an effective exposure time of around 5 minutes over the ∼5 hr of observation time. In preparing data for DEM analysis, the NuSTAR rate (in each region, time interval, and energy range) was corrected for instrument livetime to extract the expected true incident rate. The input uncertainties for each NuSTAR channel were found by adding 20% of the observed rate in quadrature with statistical uncertainties based on the number of observed NuSTAR events.

In order to calculate the NuSTAR temperature responses, it is necessary to combine the expected X-ray spectrum from a thermal source with the NuSTAR instrument response in a given energy range. To find the former, a catalog of simulated X-ray spectra for plasma of different temperatures was generated using `f_vth.pro` (available in the SSWIDL XRAY library). This photon model uses CHIANTI coronal abundances (v9.0.1; Dere et al. 1997, 2019) and includes the thermal bremsstrahlung continuum as well as spectral lines which appear in the energy range under consideration (2.5–10 keV). For the latter, the NuSTAR analysis pipeline was used to generate spectral data products which contain information about the response of the instrument to incoming emission, including the energy-dependent effective area, detector response, and other factors.[12] These are combined with the simulated thermal emission spectra as a function of temperature to generate a distinct temperature response function for every NuSTAR energy range.

In order to take advantage of all information available, data and responses from both NuSTAR telescopes (FPMA and -B) were summed in each energy range.

---

[10] https://xrt.cfa.harvard.edu/resources/documents/XAG/XAG.pdf

[11] In terms of NuSTAR event grades, we select events of grades 0–4 for inclusion in DEM analysis, and correct for pileup by subtracting 1.25× the observed spectrum in grade 21–24 events.

[12] Specifically, the `nuproducts` module.
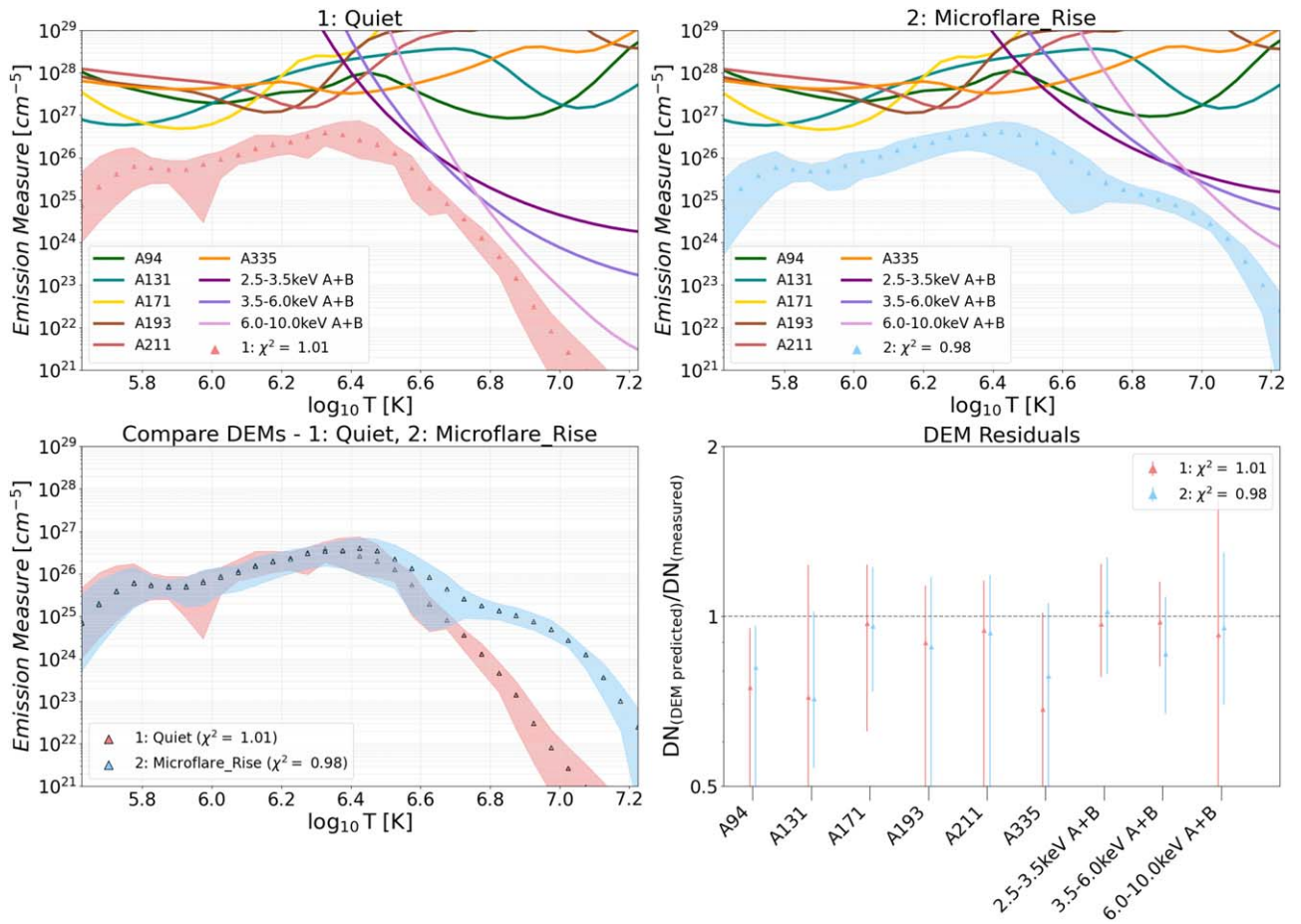
Figure 3. Results from DEM analysis of example intervals which represent extrema of the behavior of the region. EMD distributions are shown with shaded uncertainty regions giving the range of solutions found in all DEM iterations (see Section 3.1). Top left: a quiet time (20:51:30–20:54:30 UTC). Top right: the impulsive phase of the largest microflare (16:22:15–16:22:45 UTC). Loci curves from each instrument involved are included in the top two panels. Both example DEMs are from times outside of the XRT data intervals, so no XRT data were used. Lower left: direct comparison. The quiescent interval (red) shows significantly less plasma at higher temperatures than is present during the impulsive phase of a microflare (blue). Lower right: residuals. DEM-predicted observations in each instrument, divided by the actual input.

Prior NuSTAR studies involving spectroscopy of solar microflares have determined that there is a discrepancy in the NuSTAR gain that arises in the extremely high-count-rate (low-livetime) regime associated with observations of brighter solar sources. This discrepancy and a method used to correct for it in spectroscopy are presented in Duncan et al. (2021). In this analysis, it was not found to have an appreciable effect on DEM results, so no correction was applied to the NuSTAR inputs. The implications of the gain discrepancy for NuSTAR DEM studies are discussed further in Appendix C.

3.3. Time Interval Selection

We require at least 10 actual (not livetime-corrected) counts in NuSTAR in each energy range in each DEM time interval to achieve sufficient statistics for proper use of the DEMREG method. As discussed in Section 3.2.3, limited NuSTAR livetime (range 0.2%–4%; average ∼2% over this observation) means that the number of actual counts recorded by the instrument is far below the livetime-corrected estimate of the incident photon rate.

In order to take advantage of better high-energy NuSTAR statistics at more active times while still integrating sufficiently long at quieter times, we calculate DEMs at an adaptive cadence. DEM intervals are at minimum 30 s in duration, and at

maximum extend in duration however long it takes for the instrument to record 10 actual NuSTAR counts between 6 and 10 keV (sometimes several to ∼10 minutes). This results in 170 total time intervals over the ∼5 hr of NuSTAR observing time.

As AIA takes full-disk images in all of its EUV channels every ∼12 s (Lemen et al. 2012), there are unique AIA data in every interval. During the intervals where XRT observed during the NuSTAR orbits, usable (nonsaturated, full-resolution) images in each filter are available around every minute. However, due to the sparseness of the intervals with overlapping NuSTAR/XRT coverage (see Figure 1), we do not make it a requirement to have a XRT image in every DEM interval. See Appendix A for discussion of the role of XRT in constraining the DEM when NuSTAR is also in use.

4. Results

Figure 3 shows the EMD resulting from DEMs evaluated during two time intervals: one where the AR was quiescent, and one during the impulsive phase of the largest observed microflare. Loci curves are shown (observed data divided by the instrument temperature-dependent response) for each of the instruments observing in the two time periods. Each of these curves forms a constraint on the DEM distribution. As expected, the microflare EMD shows significantly more plasma
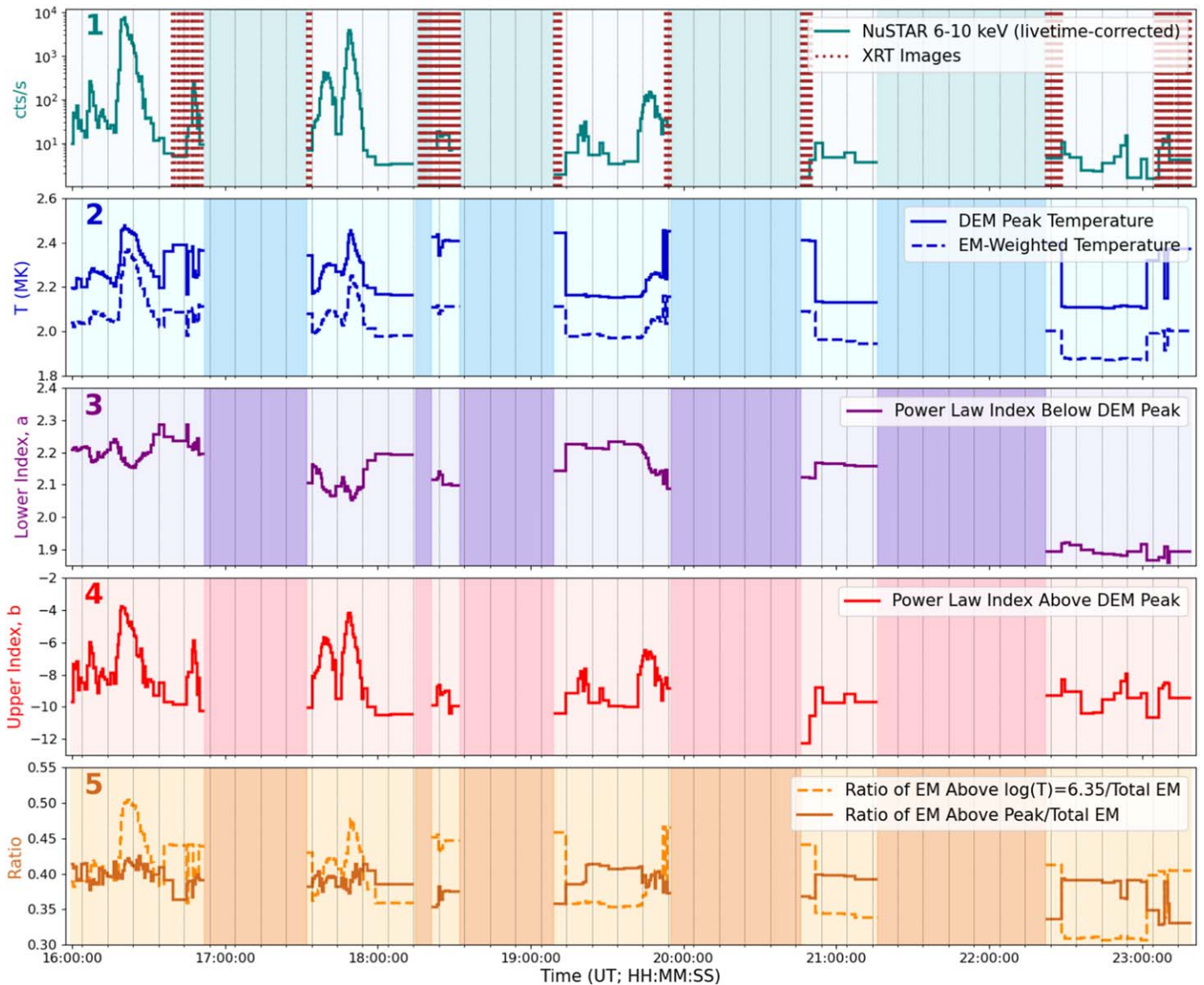
Figure 4. Evolution of the active region during the observation interval, as shown via parameters extracted from the resulting EMD at each time. Light and dark vertical shaded blocks indicate NuSTAR data availability, and dashed red lines in the top panel indicate times with both NuSTAR and XRT data available. (1) NuSTAR lightcurve (livetime-corrected, 6–10 keV counts only), shown in log scale to emphasize much fainter transients in the later orbits as well as the larger microflares. (2) Temperature of EMD peak (found via Gaussian fitting), and emission-measure-weighted temperature over entire DEM interval (see Equation (4)). For discussion of peak temperature (and other parameter) discontinuities between XRT/no-XRT times, see Appendix A. (3) Index of power-law fit to EMD curve between $\log(T) = 6$ and 6.35. (4) Index of power-law fit to EMD curve above peak. (5) Total EM above the DEM peak temperature divided by total EM over entire temperature range, as well as total EM above a reference temperature ($\log(T) = 6.35$) divided by total EM over entire temperature range.

at higher temperatures than the quiescent example, while the distributions are more similar at lower temperatures.

In the next subsections, we discuss the DEM results across *all* time intervals. In Section 4.1, we introduce parameters extracted from the EMD and discuss their evolution throughout the observation interval. In Section 4.2, we highlight the evolution of the EMD during a microflare. Finally, Section 4.3 discusses evidence for (and evolution of) higher-temperature components over time.

4.1. Full-observation DEM Evolution

In order to understand the evolution of the AR EMDs throughout our observations, we extract a number of parameters describing aspects of the structure of these distributions. Figure 4 summarizes the behavior of these

parameters over the course of the full AR observation. Panel 1 of Figure 4 shows the NuSTAR livetime-corrected 6–10 keV lightcurve.

4.1.1. EMD Peak and Emission-measure-weighted Temperatures

The peak of the EMD (Figure 4, panel 2) is found between 2 and 2.6 MK consistently over the evolution of the AR. Increases in peak temperature are seen during larger transients, which heat enough plasma to shift the peak of the thermal distribution of the AR as a whole. This peak temperature is somewhat lower than that found in the bulk of prior AR DEM studies with EUV and/or SXR instruments (a range of studies find ∼3.2–4 MK; Warren et al. 2012). This result is expected, as this analysis includes a much broader spatial region (motivated by NuSTAR's limited spatial resolution; see

Section 3.2.3), rather than only a small portion of the AR core, as is common practice when the instruments in use have higher spatial resolution (e.g., Warren et al. 2016). The alternate DEM calculations using `xrt_dem_iterative2.pro` found a similar range of peak values.

The emission-measure-weighted temperature ($T_{\rm EM}$) is also shown in panel 2, defined as

$$T_{\rm EM} = \frac{\int_T {\rm EMD} \times T}{\int_T {\rm EMD}}, \tag{4}$$

where the integrals may run over any range of temperatures where the DEM is defined (values shown in Figure 4 were found via integration over the full temperature range). Like the peak, we see this value shift upwards during transients. Discontinuities in the time evolution of the peak temperatures are seen between times with and without XRT data available; see Appendix A for discussion of the effects of XRT on the DEM.

4.1.2. EMD Power-law Rise/Decay

In addition to the two characteristic temperatures, we also examine the slopes of the EMD distribution above and below the temperature peak. We fit expressions of the form EM $\propto T^a$ (EM $\propto T^{-b}$) to the distribution below (above) the peak. In Figure 4, panels 3 and 4 show the indices (a, $-b$, respectively) found from fits to the EMD in each time interval.

The lower power-law index (a) is related to the frequency of heating events occurring in AR loops, as well as the loop length (Cargill 2014). Here, a is fit between $\log(T) = 6$ and 6.35 (1 to $\sim$2.2 MK), and is found to range from $\sim$1.9 to 2.3 over the course of the observation, which is on the low end of the values found in prior EUV/SXR studies of AR cores ($2 < a < 5$, as summarized in Table 3 of Bradshaw et al. 2012, and which informed the analysis of Cargill 2014). This result is consistent with the inclusion here of more lower-temperature material from outside the core. At flare times, a dips downward, as heating of initially cooler material from subpeak to superpeak temperatures leads to a more gradual slope up toward the peak.

There are considerably lower values of a seen during the final orbit. These low values occur because the DEM is strongly constrained by the 171 Å AIA channel in the lower part of the temperature range (see Figure 2), and that channel sees a significant rise in emission during the final NuSTAR orbit (see Figure 1) as a result of a transient that appears primarily in AIA 131 and 171 Å alone.

Finding the power-law index (b) of the decaying EMD above the peak provides a way to characterize the highest-temperature portion of the distribution, which is also crucial for investigating heating mechanisms. This index ranges widely during this observation (from $\sim$4 to 12), decreasing significantly during flaring intervals with more observed NuSTAR emission, as was also seen in the FOXSI-2 flare DEMs in Athiray et al. (2020). The evolution of the upper index closely follows the NuSTAR high-energy (6–10 keV) lightcurve (as shown in panel 1 of Figure 4), because that measurement is the strongest constraint on the high-temperature DEM. The range of index values found here includes the range 7–10 previously reported (Warren et al. 2012; Barnes et al. 2016b).

4.1.3. Total Emission Measure Above/Below Peak

Panel 5 in Figure 4 shows the ratio of the total EM integrated above the peak and the total EM integrated over the full temperature range, i.e., the percent of material that is at temperatures above the peak as a function of time. We see that the higher-temperature material consistently makes up about 40% of the total EM in the entire AR, with minor enhancements when more plasma is heated in a few of the larger flares. The peak itself shifts higher in temperature at flare times, so any flare-associated enhancement in this value indicates a significant increase in material at the highest temperatures (not just a shift in the distribution around the peak). For comparison, the percent of emission above a reference temperature ($\sim$2.2 MK) is also shown in this panel. This latter metric *is* influenced by the shift in peak location.

Discontinuities in the time evolution of these parameters are also seen at the beginning and end of the XRT times (see Appendix A).

4.2. Microflare Evolution

In Section 4.1, we noted several EMD-extracted parameters that are modified at microflare times. Figure 5 shows the evolution of all parameters during a microflare. In the upper panel of Figure 5, quantities from Figure 4 are shown on the same axes. In the lower panel of Figure 5, the total EM integrated above three threshold temperatures (5, 7, and 10 MK) are shown, along with the NuSTAR 6–10 keV lightcurve.

Moving chronologically through the flare, the NuSTAR 6–10 keV count rate and upper power-law index (b) are the first parameters to show flare-associated enhancement. This time period corresponds to an initial rise in the amount of plasma in the very highest temperatures. Next, we see the peak temperature, EM-weighted temperature, and the EM curves in the lower panel begin to rise as more plasma is heated. Additionally, we see the lower power-law index (a) decrease, which shows broadening of the EMD peak.

The NuSTAR 6–10 keV lightcurve peaks before the EM curves, which then each peak successively in time (higher-temperature thresholds peak earlier). In other words, the amount of plasma heated to the highest temperatures peaks before that heated to relatively lower temperatures. The NuSTAR 6–10 keV peak occurring before any of the EM curve peaks likely indicates the presence of significant plasma >10 MK in the rise/peak portion of this microflare (see additional evidence of this in Section 4.3.2).

We additionally see enhancement in the EM ratio during the flare, meaning that the total fraction of plasma above the EMD peak becomes an increased percentage of the total plasma distribution (by $\sim$4%). This occurs despite the fact that the peak itself increases in temperature (which, on its own, would oppose an increase in this ratio). The EM ratio peaks latest of any of the extracted parameters shown, indicating that the total amount of plasma heated above the peak temperature continues to increase even as the high-energy emission and hotter components are in decay.

These results are all consistent with an initial energy release to heating of a small, hot volume, with later transfer of energy to more broad heating in the AR. In Section 4.3, we will examine the evolution of the hot side of the distribution in more detail.
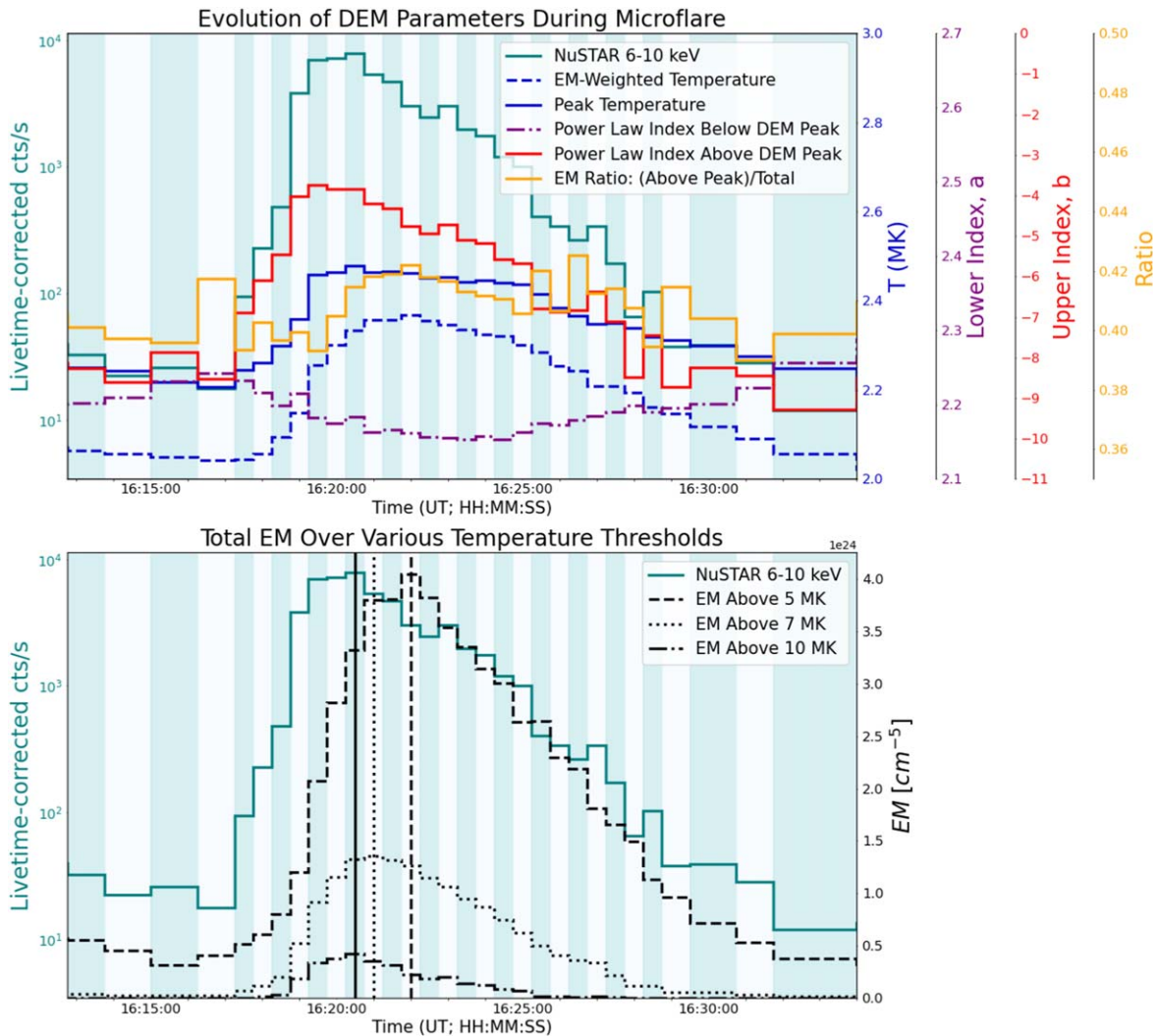
Figure 5. Evolution of extracted parameters over a single microflare. Background light and dark shades are used to highlight the individual DEM time intervals in use. Upper: all parameters from Figure 4 are shown over the flare interval, with several additional color-coded vertical axes defined to the right. Lower: total EM (EMD-integrated) above three threshold temperatures are shown in conjunction with the NuSTAR 6–10 keV livetime-corrected lightcurve.

4.3. DEM Characterization of the Hottest (>5 MK) Active-region Plasma

Figure 6 shows the evolution of the DEM-estimated amount of plasma (in line-of-sight EM) above certain temperature thresholds as a function of time, with uncertainty ranges on the EM values from the iterative process described in Section 3.1. The time evolution of the amount of material above these thresholds shows a close correspondence to the NuSTAR 6–10 keV lightcurve, as expected given the strength of that constraint in these temperature ranges. The amount of material above each threshold is enhanced both at identified microflare times, as well as in conjunction with smaller apparent X-ray transients.

Looking in particular at the >10 MK EM, we compare the results to the estimated amount of >10 MK plasma found by Ishikawa et al. (2017) in their FOXSI-2 study of AR 12234 during a quiescent interval. They estimate 1.8×10^{22}–1.5×10^{23} cm^{-5} above 10 MK. We see that AR 12712 possesses similar amounts of >10 MK plasma only during larger micro-flares, and that ∼2–4 orders of magnitude less >10 MK material is estimated to be present during quiet times ($<10^{20}$ cm^{-5}; later results in Section 4.3.2 show us these data are actually consistent

with *no* >10 MK emission). This order of difference was found using both the DEMREG and `xrt_dem_interative2.pro` methods (DEMREG results shown).

In the next two subsections, we examine the hottest material in this AR in more detail. Section 4.3.1 traces out the time evolution of the relationship between the amount of >5 MK plasma and the emission-measure-weighted temperature, and Section 4.3.2 varies the temperature range used for the DEM calculation in each interval, to investigate whether the inclusion of material above certain thresholds is necessary for a good DEM solution.

4.3.1. Total Emission Measure versus Emission-measure-weighted Temperature

Here, we consider the evolution of the >5 MK material in the AR, particularly examining the interplay between how much plasma is observed above that threshold (total EM, found by integrating the EMD distribution from ∼5.0 to 15.8 MK), and the emission-measure-weighted temperature above that threshold (T_{EM}, found by evaluating Equation (4) with both sums taken over that same range). Figure 7 illustrates the
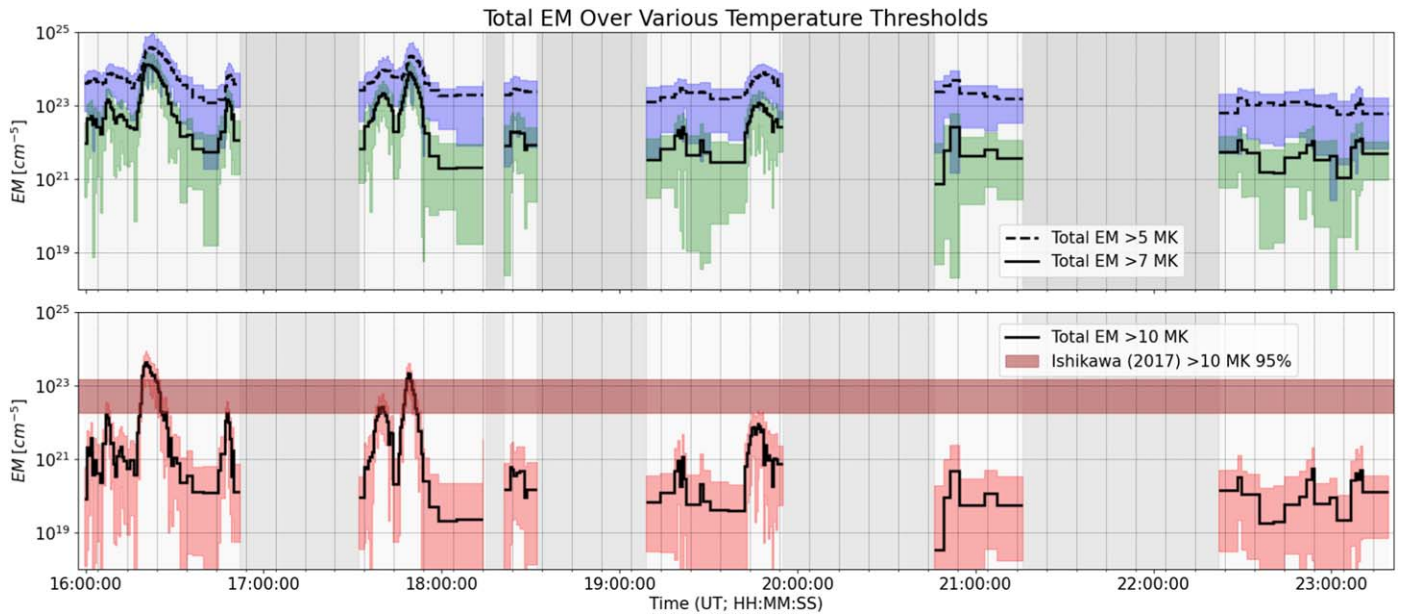
Figure 6. Total EM in the EMD as integrated above certain temperature thresholds, shown as a function of time. Upper: total EM over 5 (7) MK, shown as dashed (solid) histogram with blue (green) uncertainty range. Lower: total EM over 10 MK, also shown with uncertainty range (pink). Horizontal bar shows the estimated range of the amount of >10 MK plasma found via DEM analysis of a quiescent AR observed by XRT and FOXSI-2 (Ishikawa et al. 2017; range: their DEM solutions with chi-squared values within 95% occurrence probability).

motion of the distribution through the phase space defined by these two quantities as a function of time.

The top panel of Figure 7 shows these values for all 170 DEM intervals. Points are colored with respect to their order in time, with a corresponding time-stamped color bar and a NuSTAR lightcurve serving as a key in the panel immediately below. Additionally, the duration of each DEM interval is expressed via the size of the markers, with longer-duration DEMs (in quieter times; see Section 3.3) appearing as comparatively larger circles. We see that points from quiet times are grouped toward the bottom left, indicating relatively small amounts of plasma above 5 MK, as well as a low emission-measure-weighted temperature. At times of transients, there are excursions up and to the right.

To highlight transient behavior, the lower set of panels shows the time evolution during specific intervals (highlighted and numbered in the lightcurve). To allow comparison of the shape of the evolution between transients, the aspect ratio of these plots is held fixed to that of the top plot (though the plot limits change to better highlight the behavior of transients of different magnitude). For the larger transients (labels 2 and 5, B- and mid-A-class microflares, respectively), arrows indicate the counterclockwise path the EMD follows through this space, starting at the lower left.

Examining the larger events, we see that the >5 MK portion of the EMD shows an initial sharp increase in $T_{\rm EM}$ with a smaller simultaneous increase in EM. This change indicates that *the initial heating occurring in the microflares is heating of material that is already relatively hot*. Later in the evolution of these events, there is a much sharper rise in EM while $T_{\rm EM}$ actually decreases. This suggests later heating of much more material that was initially cooler, consistent with a picture involving a rise in density in coronal loops later in the flare evolution, once flare-heated chromospheric material evaporates upward.

During quiet times and smaller transients (smaller- and sub-GOES-Aclass activity), we see initial increases predominantly

along the $T_{\rm EM}$ axis, with lesser enhancement of total EM, followed by a corresponding decay back to the preflare condition. These smaller transients repeatedly trace out similarly shaped diagonal paths in this space, indicating that over the course of this observation plasma heating follows a similar process in events across a range of scales.

4.3.2. Variable-temperature-range DEMs

The temperature range over which the DEM is calculated in the bulk of this analysis is log(T) = 5.6–7.2, or ∼0.4–15.8 MK. The lower bound was chosen to include the peaks of the response of all the included AIA channels (see Figure 2). The upper bound was chosen to extend a bit above the temperatures often seen in NuSTAR spectroscopy of similar-magnitude transients (often around 10 MK). We are interested to explore whether allowing plasma at temperatures up to 15.8 MK is really necessary for a result that is in good agreement with the inputs, particularly the 6–10 keV NuSTAR emission, which provides the most rigorous high-temperature constraint. To examine this, we rerun DEM analysis for every interval using three additional upper bounds on temperature: ∼5, ∼7, 10, and ∼12.6 MK,[13] respectively. For each new solution, we record whether the DEM-predicted data is consistent with the actual NuSTAR input data in the 6–10 keV bin within uncertainty.

Before completing these variable-temperature-range DEMs, we note a property of the existing results that has the potential to affect this analysis: Across time intervals, there is a tendency for DEM residuals to trend, on average, slightly below 1 (visible, for example, in both cases presented in Figure 3). This indicates that the DEMREG method results in DEM-predicted emission of slightly lower magnitude than the actual observations, equivalent to a slight underestimate in the amount of material present across the temperature range.

---

[13] Explicitly, log$T$ = 6.7, 6.84, 7, and 7.1.
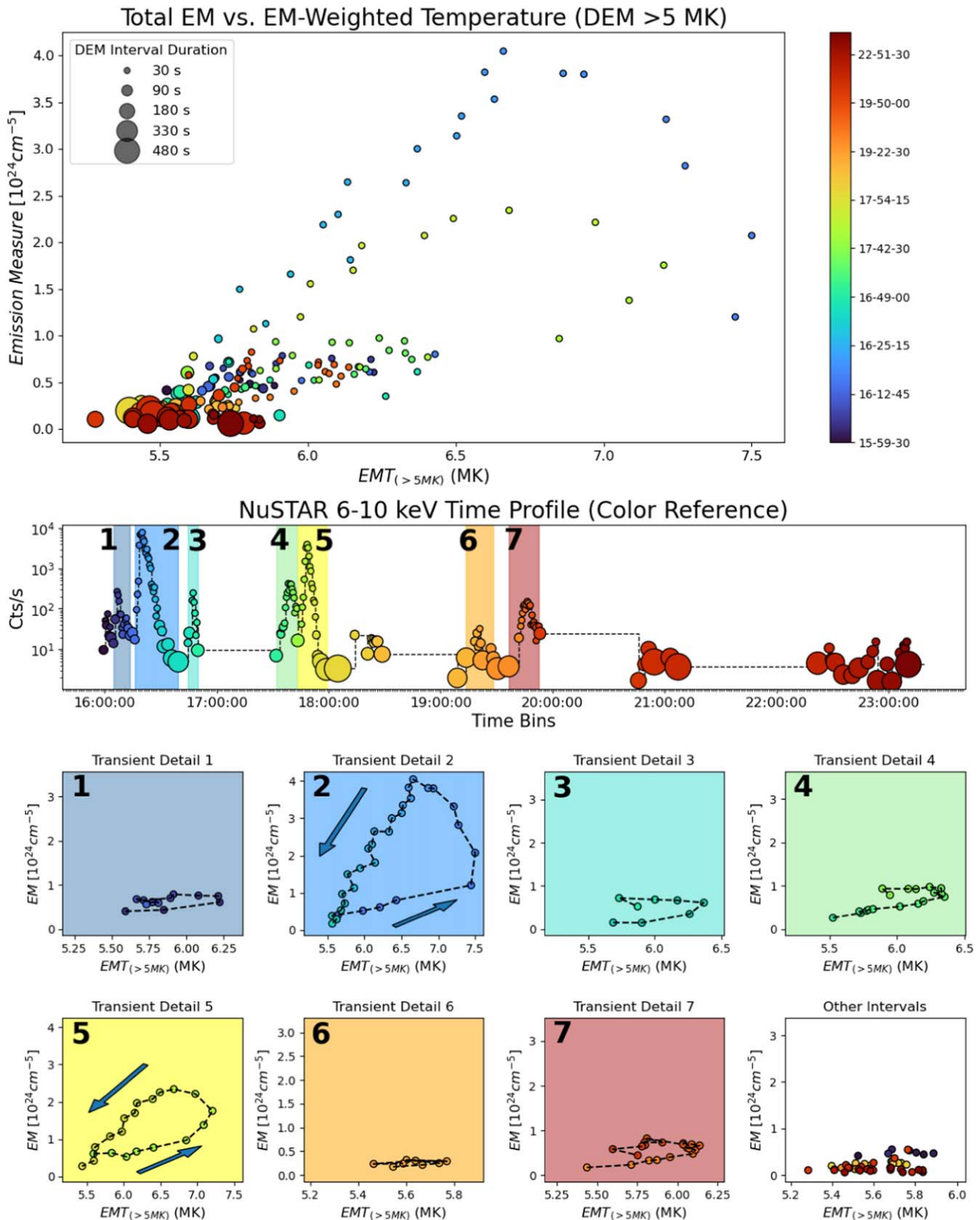
Figure 7. Evolution of the relationship between the total emission measure (EM) above 5 MK and the EM-weighted temperature calculated above 5 MK (see Equation (4) and discussion in Section 4.3.1). Values from all DEM intervals are shown in the top panel, with transient intervals highlighted in the lower small panels. For the two largest transients (2, 5), arrows indicate the direction of the evolution in time, which starts and ends at the lower left. The smaller transients evolve in a similar counterclockwise fashion. Colored points indicate time evolution. In the top plot, the size of each point indicates the duration of the DEM interval. The central panel shows the NuSTAR 6–10 keV rate during each DEM interval, with the same point colors and sizes for reference in interpreting the time evolution of the quantities above and below.
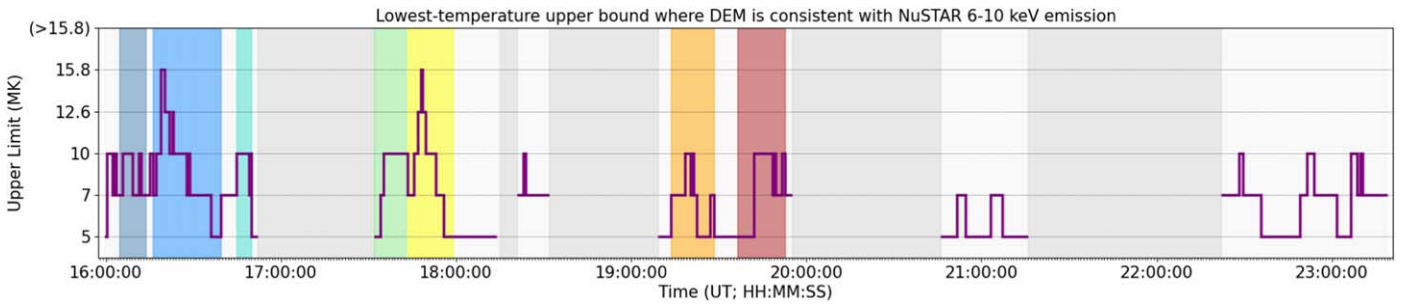
Figure 8. Results from varying the temperature range over which the DEM is calculated by lowering the upper limit. Restricting the highest temperature allowed in the DEM often causes inconsistency between the DEM-predicted and real input data in NuSTAR 6–10 keV. This figure shows the lowest upper-bound temperature at which the DEM-predicted 6–10 keV NuSTAR emission is consistent with the actual observed emission within uncertainty (see Section 4.3.2). At the quietest times, a DEM over a temperature range that extends only up to 5 MK is consistent with observations, but during transients a broader temperature range is necessary for agreement. The same transients highlighted in Figure 7 are highlighted here via multicolored shading.

A constant factor $f = \frac{1}{n} \times \sum_r \frac{1}{r}$ is found from the n original residuals, r, which is multiplied by the EMD to find a new solution with DEM-predicted residuals more uniformly distributed around 1. Comparing results with and without this EMD scaling factor across all prior sections of the paper, we see no significant effect on our conclusions. This is because the rescaling is constant across temperature (so does not effect the DEM shape), and is of small magnitude with respect to the EMD (we always find $1 < f < 2$).

However, we do find the application of this correction factor necessary for the variable-temperature-range DEM analysis, as the rescaling by design has a more significant effect on the residuals themselves, and we are directly utilizing the NuSTAR 6–10 keV residual to determine if we see evidence for material above a given temperature range. We specifically apply the constant factor f from the DEM over the full temperature range ($\log(T) = 5.6$–7.2) to the results using all other temperature ranges; this is to avoid distortion observed when f is calculated from a poor DEM solution (which we expect here, as we intentionally restrict the temperature range to determine when the DEM fails to find a good solution).

In Figure 8, we show the lowest-temperature upper bound where the DEM-predicted data is consistent with the NuSTAR 6–10 keV input, within uncertainty, as a function of time. At quieter times, a DEM over a range extending only up to 5 MK might produce a consistent result, but during more active intervals allowing plasma up to higher temperatures is clearly needed. We find that allowing material above 10 MK is necessary in two out of seven of the marked microflares (colored shading), specifically in the two largest events.

A change from coronal- to photospheric-like elemental abundances has sometimes been observed in flares, including microflares of similar brightness to these events (e.g., Rao et al. 2023). In addition to the Bremsstrahlung continuum, NuSTAR has sensitivity to spectral lines from elements with low first ionization potential, which are comparatively less abundant in the photosphere.[14]

While NuSTAR has limited ability to directly measure changes in abundance, we can examine the possible effects of a flare-time shift toward photospheric abundances on the highest-temperature components of the DEM. To do so, we rerun the analysis of this section with modified NuSTAR responses, calculated with the assumption of photospheric abundances. This leads to a factor of $\sim$2 greater amount of material

$>$10 MK than the coronal assumption, and to the requirement of material between 10 and 12.6 MK during one additional microflare (the chronologically fourth; green in Figure 8).

The higher-temperature spectral components found via spectroscopy of these microflares in Duncan et al. (2021) were $\sim$10 MK. Comparing this to the $>$10 MK components identified here, we stress that these results are not inconsistent. Rather, they reflect the fact that spectroscopy of a thermal plasma distribution using isothermal models extracts characteristic temperatures representing what is in fact a complex, multithermal distribution. DEM analysis provides more detailed information about the thermal distribution, and suggests that in some of these events there is a notable extension above 10 MK—in fact, the two brightest events even briefly require material above 12.6 MK.

Even outside of the confirmed microflaring times (during quiescent times, and small X-ray transients that are much too faint to be seen in GOES) there are intervals where plasma above 5 or 7 MK is needed for a solution consistent with the NuSTAR observations. However, there are no intervals outside of microflares where $>$10 MK material is necessary. This, again, contrasts greatly with the results of Ishikawa et al. (2017), where a significant amount of $>$10 MK material was identified in a different quiescent AR.

5. Discussion

The objective of this analysis was to examine the thermal distribution of plasma in AR 12712 through both flaring and nonflaring times, via time-resolved DEM analysis. We first discuss our results in conjunction with prior literature involving quiescent AR DEMs.

The range of values found for the upper power-law (b) fit to the EMD decay above the peak intersected with the range of values found in other works, as summarized in Barnes et al. (2016a). We note that the second paper in that series (Barnes et al. 2016b) includes discussion of the challenges of meaningful interpretation of this index, due to departure of the EMD from a power-law relationship. This departure leads to a high sensitivity of the fit to the chosen range of temperatures over which it is calculated. We observed similar issues in this analysis.

Several parameters describing the EMD distribution (peak temperature, rise index a) deviate from the established literature using EUV and SXR instruments. The EMD peak was found consistently between 2 and 2.6 MK over the observation interval, distinct from both the $\sim$3.2–4 MK found in a range of prior EUV/SXR studies of other regions (Warren et al. 2012)

---

[14] Ca XIX ($\sim$3.9 keV), and the $\sim$6.7 keV Fe complex.

as well as the 4 MK peak found by Warren et al. (2020) for *this* AR using EIS, XRT, and AIA. Similarly, *a* was found to range between 1.9 and 2.3 over the course of the observation (compare to the range $2 < a < 5$ presented in Bradshaw et al. 2012).

These differences are consistent with the fact that a larger portion of lower-temperature material in the AR is included in our DEMs, rather than just the AR core. This lower-temperature material is a consequence of the large spatial regions chosen for analysis, motivated by the comparatively poor spatial resolution of NuSTAR. This limitation is a consequence of NuSTAR's specific design; improved resolution (5″ FWHM) has been achieved with FOXSI-3, and even higher resolution focused HXR instruments are currently in development (Buitrago-Casas et al. 2021).

Due to the highly distinct magnetic environment of the AR core with respect to the outskirts of the AR or surrounding quieter regions, it is reasonable to assume that heating processes may proceed very differently between these coronal features. This strongly motivates the implementation of future focused HXR instruments that combine high sensitivity with improved spatial resolution, allowing independent measurement of the thermal distribution of the AR core (as opposed to the combination of the core and its surroundings).

Considering the hot side of the EMD, we found significantly less >10 MK material in this region at quiescent times than was found in the quiescent AR analyzed by Ishikawa et al. (2017; $<10^{20}$ versus $>10^{22}$ cm^{-5}). The larger region used in this analysis (by a factor of ∼8; here, circular with radius 150″, versus their 100″ square region) contributes to this discrepancy: Since more hot plasma is expected to be located in the AR core, the use of a larger region including parts of the AR with little high-temperature material has the effect of depressing the line-of-sight EM at high temperatures (essentially, a spatial average of the EM across the entire region under consideration). However, this cannot fully explain the difference. Estimating that the AR core takes up roughly 10% of the area in our region, and assuming that *all* material >10 MK exists in the AR core alone, there would only be a difference of 1 order of magnitude in the amount of >10 MK plasma found in our region versus a hypothetical "AR-core-only" DEM analysis using a higher-resolution HXR instrument. If >10 MK material exists outside the AR core, the difference would be even smaller. This suggests that the distribution of thermal plasma in this region is fundamentally different than the region observed by Ishikawa et al. (2017).

In Marsh et al. (2018), the observed properties of the AR studied by Ishikawa et al. (2017) were found to >99% confidence to be consistent only with models involving low-frequency (nanoflare) heating, rather than high-frequency heating. Our AR was subject to similar modeling efforts in Warren et al. (2020), which concluded that high-frequency heating was most consistent with their observations (EIS, XRT, and AIA observations made during 18:56–19:01 UT between two NuSTAR orbits). The significantly lower amount of >10 MK plasma found in this analysis in comparison to Ishikawa et al. (2017) makes our results qualitatively consistent with that conclusion, but a rigorous determination would require a comparison between modeling results and the DEM derived using the NuSTAR HXR observations to firmly constrain the higher-temperature material.

We additionally note the potential for the combination of similar modeling methods with observations made by future focused HXR instruments with higher spatial resolution: Achieving a HXR-constrained DEM of the AR core in combination with modeling would allow us to both infer properties of the heating processes occurring and evaluate whether the heating we see is sufficient to sustain the observed thermal distribution over time.

In examining microflare evolution, we confirm a picture wherein the event starts with the heating of a small amount of plasma to very high temperatures, followed by transfer of thermal energy to later heating of a larger amount of material to lower (yet still elevated) temperatures. This is in agreement with results from time-profile analysis in Duncan et al. (2021). Adding to this picture, the analysis of Section 4.3.1 particularly suggests that the initial plasma heating to the highest-achieved temperatures is dominated by heating of plasma that is already >5 MK. This analysis is consistent with initial energy release occurring in the hotter AR core. Later in each event, as we see a sharp rise in EM with a steady or decreasing T_{EM}, we infer that cooler material from the chromosphere is being heated and evaporating upward, increasing the density of loops in the AR core.

Strikingly, the flare-time evolution of the plasma distribution in EM versus T_{EM} space in Figure 7 has close similarities to the evolution of the plasma density as a function of temperature in prior EBTEL simulations of plasma heating in a single AR loop (compare with Figure 4 in Barnes et al. 2016a). Like larger flares, microflares at this scale are expected to involve many coronal loops rather than a single loop structure. It is intriguing that the behavior of a source consisting of a large ensemble of loops is similar to that predicted for just one. This strongly motivates future studies involving both DEMs and hydrodynamic modeling of the same events, to better understand how energy release and heating occur over a range of scales.

6. Conclusions

In this analysis, we have presented the first HXR-constrained, time-resolved DEM analysis of an evolving AR. At microflare times, we have shown a detailed picture of the thermal evolution, involving initial heating of already-hot plasma in the AR core to very high temperatures followed by later broad heating of surrounding material to cooler (yet still elevated) temperatures. At nonflaring times, we estimate that much less plasma above 10 MK (by 1–3 orders of magnitude) exists in this region than was seen in a prior HXR quiescent AR DEM study (Ishikawa et al. 2017). The significant differences between these results strongly motivate further study of additional ARs with HXR coverage at quiescent times, as it is not presently clear which (if either) of these results is typical of solar ARs as a whole. Progress toward this goal will be possible via additional existing observations made by NuSTAR (some ∼100 hr of observations made in campaigns between 2014 and 2023). A solar-dedicated focused HXR observatory capable of making these observations near-continuously (and without NuSTAR's limited livetime and spatial resolution) would allow conclusive determination of the characteristic thermal structure of solar ARs. In combination with observation-informed modeling efforts, these observations would clarify the mechanisms responsible for AR heating outside of large transients.

Acknowledgments

Appendix A
## Comparative Roles of NuSTAR, XRT, and AIA in Constraining the Differential Emission Measure

Several studies have demonstrated that DEMs using AIA and XRT alone are prone to overestimate the amount of plasma above 5 MK (e.g., Schmelz et al. 2009 and Paterson et al. 2023, as well as the differing results found by Athiray et al. 2020 and Schmelz et al. 2016 for the same region). We replicate this result: When NuSTAR constraints are not used and the DEM analysis is performed with AIA and XRT alone, the total EM above 5 MK is an order of magnitude higher than the result when using NuSTAR. This discrepancy is even more striking when isolating even higher-temperature components: the AIA/XRT-only EMD shows 2 (3) orders of magnitude more plasma above 7 MK, and 3 (4) orders of magnitude more plasma above 10 MK at a flaring (quiescent) time. Figure 9 shows results with and without NuSTAR during a quiescent interval (19:09:00–19:13:45 UTC), clearly displaying the differing behavior at high temperatures.

Examining the EM loci curves in Figures 9 and 10, it is clear that the AIA channels provide the strongest constraints at low
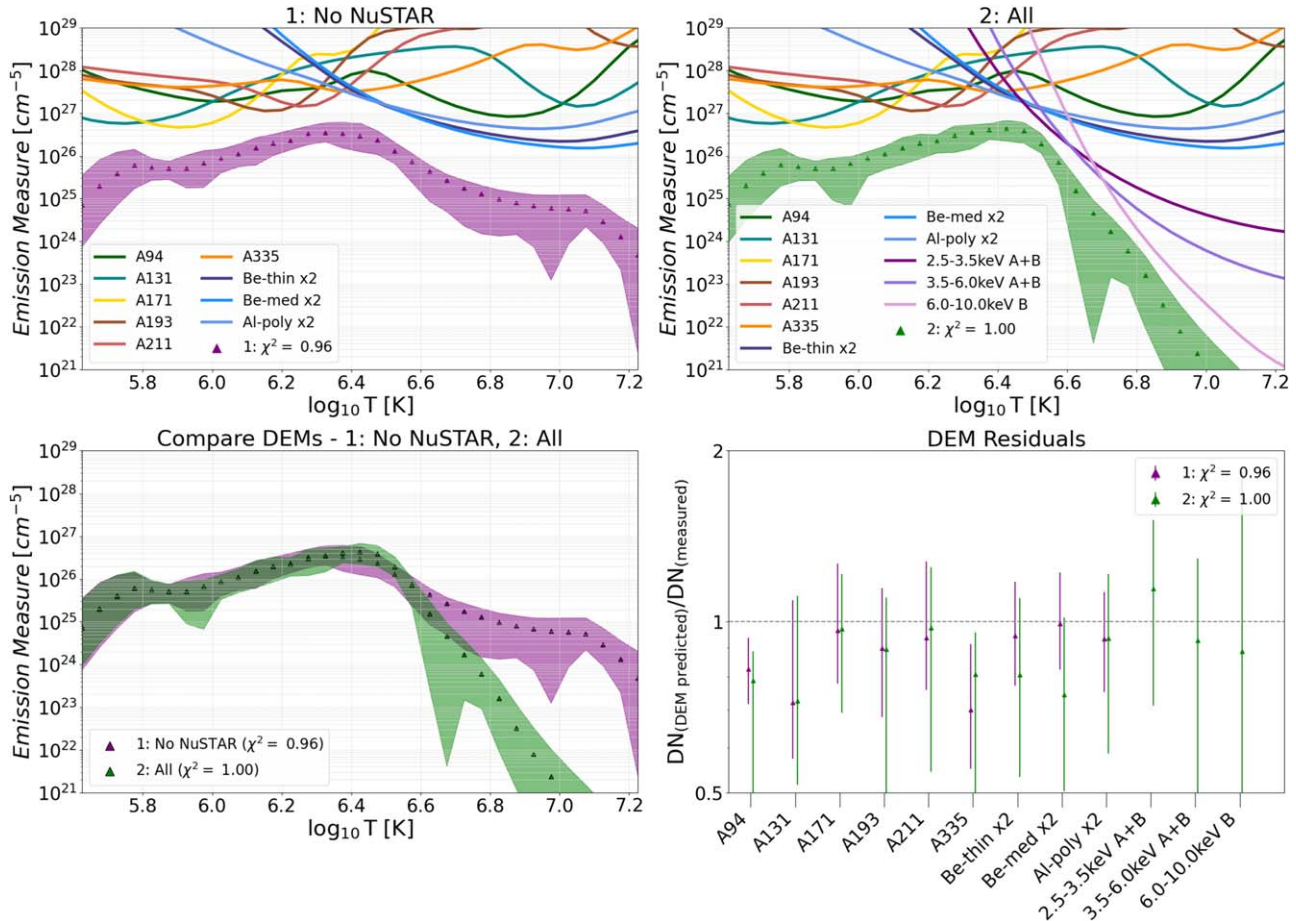
Figure 9. Comparison of DEM results during a quiescent interval (19:09:00–19:13:45 UTC) with and without the addition of NuSTAR. The high-temperature behavior of the EMD is significantly modified by the NuSTAR constraints (see discussion in Appendix A).
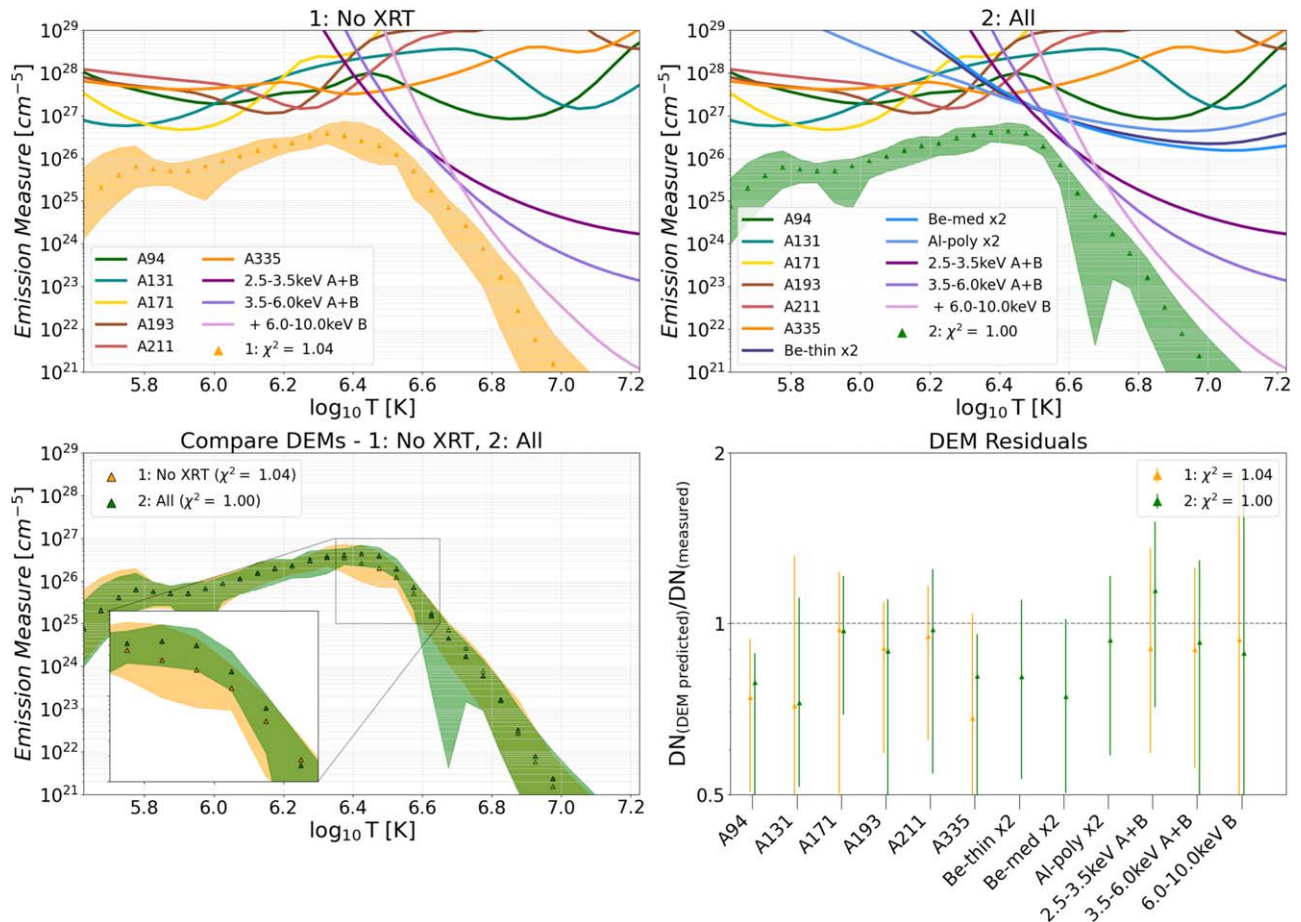
Figure 10. Comparison of DEM results during a quiescent interval (19:09:00–19:13:45 UTC) with and without the addition of XRT. While the EMDs are consistent with each other within their uncertainties over the full interval, the addition of XRT changes the solution slightly in the highest-EM region, resulting in noticeable differences in peak-associated parameters (see discussion in Appendix A and Figure 4).

temperatures, and the NuSTAR energy ranges at the highest temperatures.[15] However, there is a narrow window in temperature near the middle of the range (between $\log(T) = \sim 6.4$–6.5) where the most stringent constraint is provided by the XRT SXR filter combinations. Interestingly, this temperature is in close proximity to the peak of the EMD, and as such small changes to the constraints in this temperature range can have noticeable effects on certain output parameters.

In Figure 4, there are visible discontinuities in the peak temperature, EM-weighted temperature, and EM ratios at the transitions between intervals with XRT data included versus not. This effect is most visible in the last two orbits. Adding XRT to the DEM delivers a noticeable increase in the value of the EMD peak temperature and EM-weighted temperature, as well as a decrease in the percent of the EM that lies above the peak (a natural consequence of the former).

As the range around the peak of the EMD is where the bulk of the distribution is located, we are motivated to examine how the use of XRT can change the observed thermal energy of the plasma distribution. The thermal energy of an isothermal

plasma volume is

$$U_T = 3k_B T \sqrt{\mathrm{EM} f V}, \tag{A1}$$

where T and EM are the temperature and emission measure of the source, V is the source volume, and f is a filling factor. The DEMs in this analysis are performed over the AR as a whole, which contains many diverse plasma structures. This makes determination of the plasma volume and filling factor highly nontrivial. Additionally, it is desirable to estimate the energy of the full thermal distribution rather than a single isothermal source. To do this, we define

$$U_{T(\mathrm{arb})} \propto \frac{\int_T \xi(T) \times T dT}{\sqrt{\int_T \xi(T) dT}}, \tag{A2}$$

where $\xi(T)$ is the DEM as described in Equation (1), and we integrate over the temperature range used for the DEM calculation. Equation (A2) is a modified version of the expression for the thermal energy of a distribution of plasma given in Inglis & Christe (2014). Here, the factors f, V, and physical constants are omitted to instead give an estimate of thermal energy in arbitrary units.

Calculating $U_{T(\mathrm{arb})}$ for the same DEM intervals with and without XRT included in the DEM calculation, we find that the inclusion of XRT leads to an increase in the total thermal

---

[15] AIA has response even below the temperature range considered here; the residuals for AIA 131 and 335 Å are persistently low (actual observation underestimated by the DEM solution) due to components of their response at transition-region temperatures $<\log T = 5.6$.

energy of the distribution on the order of 10% of the energy content—a difference that, for the cases in this study, is within uncertainty.

This should be further investigated in future studies where both SXR and HXR diagnostics are available to help characterize the thermal distribution of a source; there may be significant effects on the energetics of the thermal plasma in a case where the change in input instruments modifies the EMD beyond the uncertainties defined by the DEM process.

## Appendix B
XRT Factor Comparison

A number of studies (e.g., Testa et al. 2011; Wright et al. 2017) have noted a discrepancy between EMDs derived using XRT and those derived using other instruments. This is often resolved by multiplying the XRT temperature response by a constant factor, most commonly a factor of 2. This includes recent work which used spectrally resolved SXR observations by the MaGIXS-1 sounding rocket to predict what XRT emission should be seen from the same source, and found that there was a factor of ~2 discrepancy between the observed and MaGIXS-1-predicted XRT intensity in three different XRT filter combinations (Athiray & Winebarger 2024).

Figures 11 and 12 show comparisons between DEM results using AIA, XRT, and NuSTAR with different factors used to scale the XRT response for a quiescent interval and a microflare decay interval, respectively.

The unmodified case (XRT factor 1, red) shows poor agreement with all of the XRT filter combinations, and fails to find a solution satisfying the DEMREG χ^2 condition ($\chi^2 = 1$).

When we multiply by factors between 1.5 and 3 keV (purple, blue, green), the XRT residuals move (closer) toward agreement. NuSTAR 2.5–3.5 keV (which has significant response near the temperature range where XRT is dominant) gradually changes from being overestimated by the best-fit DEM solution to being almost perfectly in line. A factor of 4 (or higher) begins to cause the opposite problem for NuSTAR 2.5–3.5 keV: The DEM solution predicts less emission than is actually observed.

We have opted to use a factor of 2 in this work, as it is both within the range of acceptable factors as seen in Figures 11 and 12, and also has been used in prior studies involving NuSTAR (e.g., Wright et al. 2017; Paterson et al. 2023), allowing ease of comparison between results from these different studies.
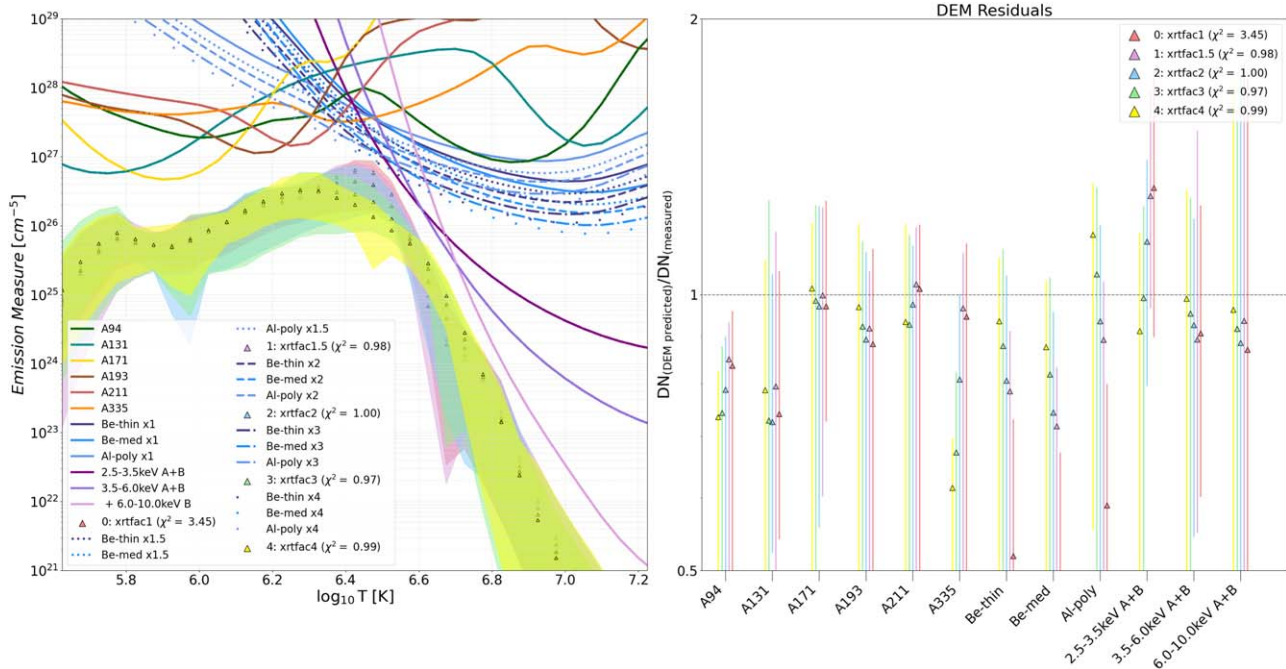
Figure 11. Comparison of DEM results with five different constant factors used to scale the XRT temperature response functions, showing the effects of this factor on the multi-instrument DEM. DEMs performed for the same quiescent interval (19:09:00–19:13:45 UTC) shown in Figures 9 and 10.
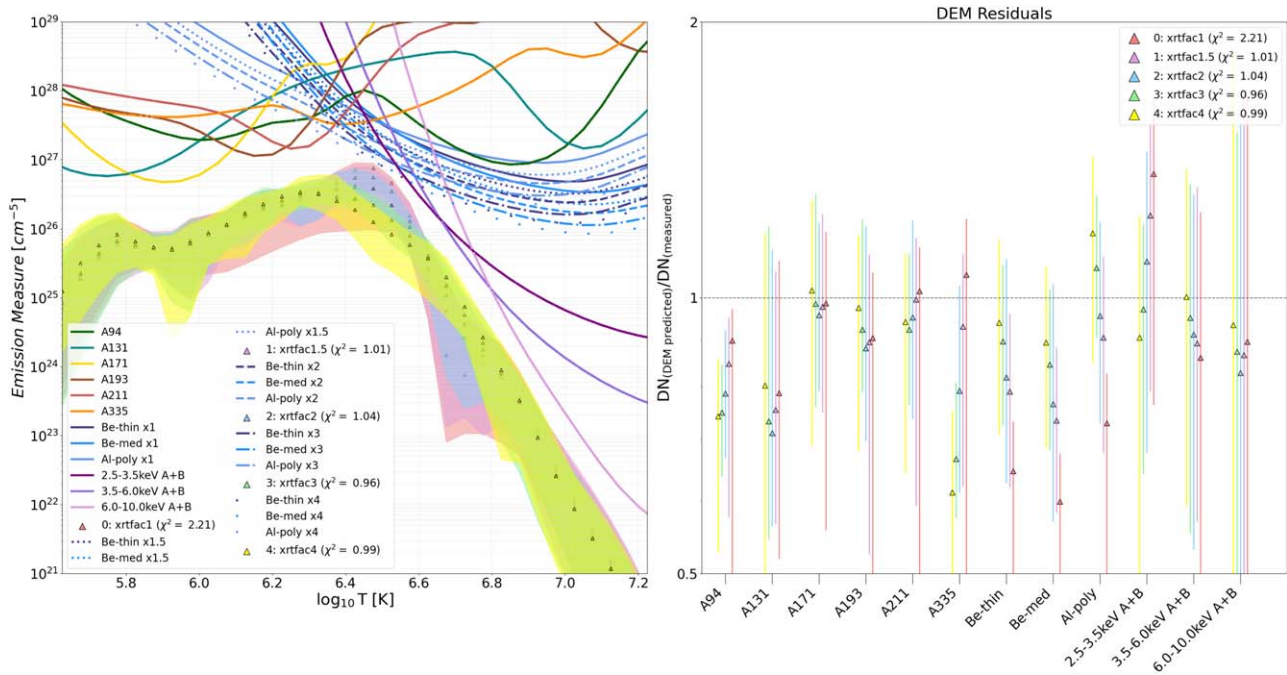
Figure 12. Comparison of DEM results with five different constant factors used to scale the XRT temperature response functions, showing the effects of this factor on the multi-instrument DEM. DEMs performed for an interval during a microflare decay (19:53:15–19:55:00 UTC).

Appendix C
Differential Emission Measures and the NuSTAR Gain Discrepancy

Spectroscopy of HXR microflares observed by NuSTAR in this and other ARs has revealed consistent discrepancies in the observed locations of known solar spectral lines. The analysis in Duncan et al. (2021; see Appendix A) concludes that this can be attributed to a small artificial shift which occurs in the NuSTAR gain during observations in the extremely high-count-rate/low-livetime regime ($>10^5$ cps, $<1\%$ livetime) experienced by the instrument during observations of bright solar sources. No gain discrepancy has been identified during observations of standard astrophysical sources, which are several orders of magnitude fainter.

The solar-specific gain discrepancy causes artificially lower energies to be observed by NuSTAR in comparison to the actual incident spectrum (for example, the strong 6.7 keV Fe complex in solar flares is often observed by NuSTAR at ~6.4 keV). A gain-correction procedure is outlined in Duncan et al. (2021) for use in HXR spectroscopy. For the events in that study (some of which are the same transients covered in this analysis), this resulted in a multiplicative (gain slope) correction to observed energies on the order of a few percent, which was applied to spectroscopy of the events during their rise/peak intervals.

For DEMs of most microflares, the process of correcting NuSTAR inputs for a gain discrepancy is straightforward. First, NuSTAR spectroscopy should be performed of the source time interval and region planned for use as a DEM input. A gain correction can be applied to the NuSTAR spectrum via the procedure described in Duncan et al. (2021). This corrected spectrum can then be used to find the NuSTAR emission observed in each energy range of interest (the NuSTAR data input to the DEM).

Figure 13 shows the results from applying a gain correction to an interval during the rise phase of the largest microflare. We see that the few-percent correction in the energies of the observed NuSTAR emission has a minimal effect on the EMD, with corrected and original cases consistent within their mutual uncertainties. In comparison to the original EMD, the corrected distribution predicts 8% more total EM above 5 MK, and 16% (19%) more above 7 (10) MK. We emphasize that because the observed gain discrepancy involves a shift to artificially *lower* energies, analysis using uncorrected NuSTAR data when this discrepancy is occurring will always find *less* hot material than is actually present.

At times when the 6.7 keV Fe complex is not a prominent feature in the NuSTAR spectrum (as is often the case at quiet times), the influence of any possible gain discrepancy is not straightforward to determine or correct. A small gain discrepancy acting on the bremsstrahlung continuum would closely resemble a similar continuum source with slightly modified temperature and EM.

Because this analysis includes quiet times where the established gain-correction procedure is not possible, and because the test gain correction in Figure 13 showed a minimal effect on the EMD, a gain correction is not included in the results presented in this study. However, there may well be cases (likely, DEMs of larger microflares) where a gain correction will be necessary for DEM analysis involving NuSTAR.
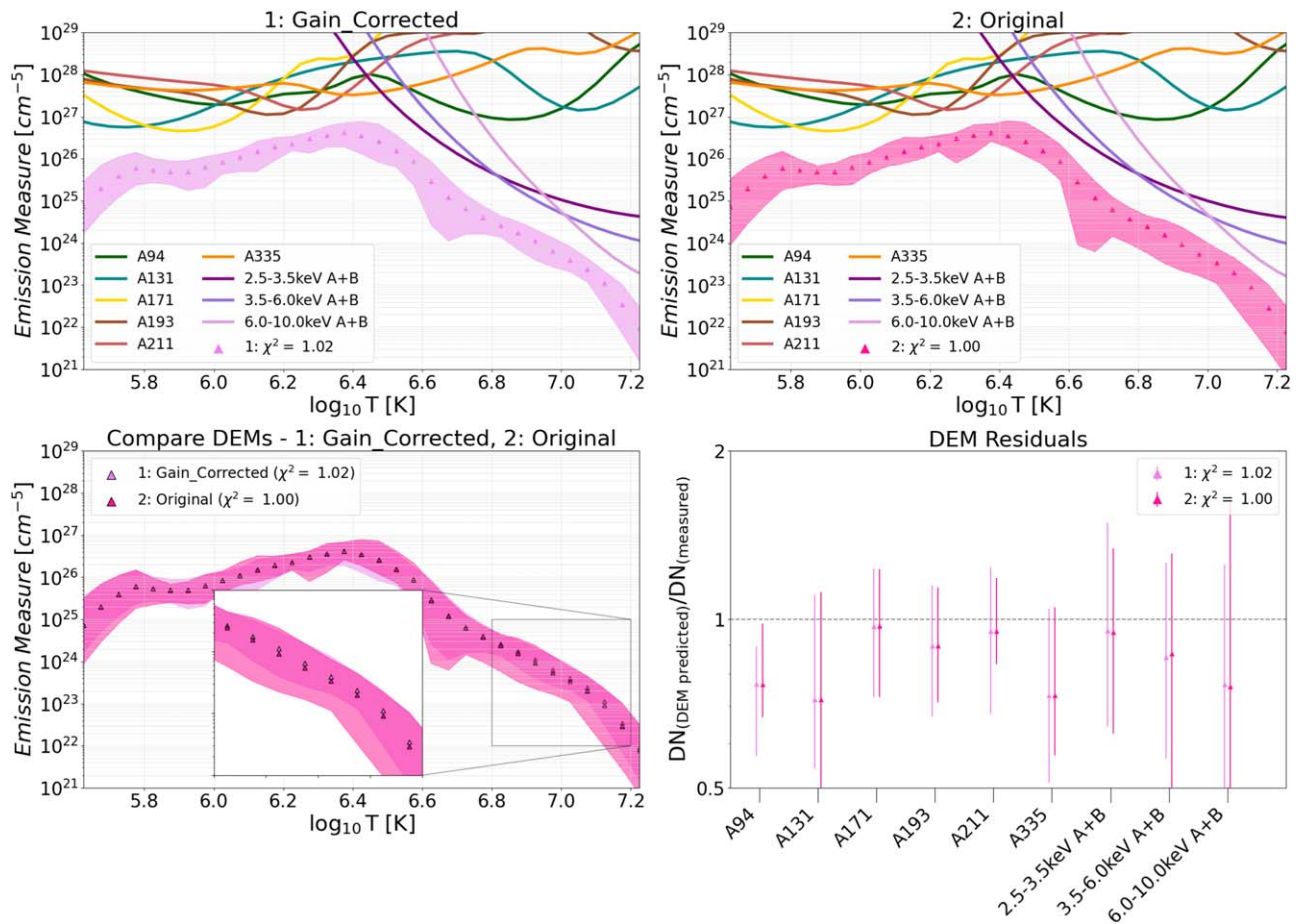
Figure 13. Comparison of DEM results during the rise of a microflare (16:18:15–16:18:45 UTC) with and without applying a correction to account for NuSTAR's gain discrepancy. The EMDs are consistent with each other within their uncertainties over the full interval, with the largest differences noticeable at higher temperatures (see discussion in Appendix C).

ORCID iDs

Jessie Duncan ⓘ https://orcid.org/0000-0002-6872-4406
Reed B. Masek ⓘ https://orcid.org/0000-0003-2395-9524
Albert Y. Shih ⓘ https://orcid.org/0000-0001-6874-2594
Lindsay Glesener ⓘ https://orcid.org/0000-0001-7092-2703
Will Barnes ⓘ https://orcid.org/0000-0001-9642-6089
Katharine K. Reeves ⓘ https://orcid.org/0000-0002-6903-6832
Yixian Zhang ⓘ https://orcid.org/0000-0001-8941-2017
Iain G. Hannah ⓘ https://orcid.org/0000-0003-1193-8603
Brian W. Grefenstette ⓘ https://orcid.org/0000-0002-1984-2932

References

Astropy Collaboration, Price-Whelan, A. M., Lim, P. L., et al. 2022, ApJ, 935, 167
Athiray, P. S., Vievering, J., Glesener, L., et al. 2020, ApJ, 891, 78
Athiray, P. S., & Winebarger, A. R. 2024, ApJ, 961, 181
Barnes, W., & Chen, B. 2022, wtbarnes/hissw: v2.0, v.v2.0, Zenodo, doi:10.5281/zenodo.6640421
Barnes, W. T., Cargill, P. J., & Bradshaw, S. J. 2016a, ApJ, 829, 31
Barnes, W. T., Cargill, P. J., & Bradshaw, S. J. 2016b, ApJ, 833, 217
Barnes, W. T., Cheung, M. C. M., Bobra, M. G., et al. 2020, JOSS, 5, 2801
Bradshaw, S. J., & Klimchuk, J. A. 2011, ApJS, 194, 26
Bradshaw, S. J., Klimchuk, J. A., & Reep, J. W. 2012, ApJ, 758, 53
Bradshaw, S. J., & Mason, H. E. 2003, A&A, 401, 699
Buitrago-Casas, J. C., Vievering, J., Musset, S., et al. 2021, Proc. SPIE, 11821, 118210L

Cargill, P. J. 1994, ApJ, 422, 381
Cargill, P. J. 2014, ApJ, 784, 49
Cargill, P. J., & Klimchuk, J. A. 2004, ApJ, 605, 911
Christe, S., Hannah, I. G., Krucker, S., McTiernan, J., & Lin, R. P. 2008, ApJ, 677, 1385
Cooper, K., Hannah, I. G., Grefenstette, B. W., et al. 2020, ApJL, 893, L40
Cooper, K., Hannah, I. G., Grefenstette, B. W., et al. 2021, MNRAS, 507, 3936
Culhane, J. L., Harra, L. K., James, A. M., et al. 2007, SoPh, 243, 19
Dere, K. P., Del Zanna, G., Young, P. R., Landi, E., & Sutherland, R. S. 2019, ApJS, 241, 22
Dere, K. P., Landi, E., Mason, H. E., Monsignori Fossi, B. C., & Young, P. R. 1997, A&AS, 125, 149
Duncan, J. 2024, jessiemcd/do-dem: Duncan et. al (2024) release, v.v2024.2.15, Zenodo, doi:10.5281/zenodo.10668572
Duncan, J., Glesener, L., Grefenstette, B. W., et al. 2021, ApJ, 908, 29
Freeland, S. L., & Handy, B. N. 1998, SoPh, 182, 497
Golub, L., DeLuca, E., Austin, G., et al. 2007, SoPh, 243, 63
Grefenstette, B. W., Glesener, L., Krucker, S., et al. 2016, ApJ, 826, 20
Hannah, I. G., Christe, S., Krucker, S., et al. 2008, ApJ, 677, 704
Hannah, I. G., Grefenstette, B. W., Smith, D. M., et al. 2016, ApJL, 820, L14
Hannah, I. G., & Kontar, E. P. 2012, A&A, 539, A146
Harris, C. R., Millman, K. J., van der Walt, S. J., et al. 2020, Natur, 585, 357
Harrison, F. A., Craig, W. W., Christensen, F. E., et al. 2013, ApJ, 770, 103
Hunter, J. D. 2007, CSE, 9, 90
Inglis, A. R., & Christe, S. 2014, ApJ, 789, 116
Ishikawa, S.-n., Glesener, L., Christe, S., et al. 2014, PASJ, 66, S15
Ishikawa, S.-n., Glesener, L., Krucker, S., et al. 2017, NatAs, 1, 771
Ishikawa, S.-n., & Krucker, S. 2019, ApJ, 876, 111
Lee, J.-Y., Raymond, J. C., Reeves, K. K., Moon, Y.-J., & Kim, K.-S. 2017, ApJ, 844, 3
Lemen, J. R., Title, A. M., Akin, D. J., et al. 2012, SoPh, 275, 17
Marsh, A. J., Smith, D. M., Glesener, L., et al. 2018, ApJ, 864, 5
McTiernan, J. M. 2009, ApJ, 697, 94

Parker, E. N. 1988, ApJ, 330, 474

Paterson, S., Hannah, I. G., Grefenstette, B. W., et al. 2023, SoPh, 298, 47

Rachmeler, L. A., Winebarger, A. R., Savage, S. L., et al. 2019, SoPh, 294, 174

Rao, Y. K., Mondal, B., Del Zanna, G., et al. 2023, ApJ, 958, 190

Reale, F., McTiernan, J. M., & Testa, P. 2009, ApJL, 704, L58

Schmelz, J. T., Christian, G. M., & Matheny, P. O. 2016, ApJ, 833, 182

Schmelz, J. T., Kashyap, V. L., Saar, S. H., et al. 2009, ApJ, 704, 863

Shimizu, T. 1995, PASJ, 47, 251

Testa, P., Reale, F., Landi, E., DeLuca, E. E., & Kashyap, V. 2011, ApJ, 728, 30

The SunPy Community, Barnes, W. T., Bobra, M. G., et al. 2020, ApJ, 890, 68

Van Doorsselaere, T., Srivastava, A. K., Antolin, P., et al. 2020, SSRv, 216, 140

Virtanen, P., Gommers, R., Oliphant, T. E., et al. 2020, NatMe, 17, 261

Warren, H. P., Brooks, D. H., Doschek, G. A., & Feldman, U. 2016, ApJ, 824, 56

Warren, H. P., Reep, J. W., Crump, N. A., et al. 2020, ApJ, 896, 51

Warren, H. P., Winebarger, A. R., & Brooks, D. H. 2012, ApJ, 759, 141

Winebarger, A. R., Warren, H. P., Schmelz, J. T., et al. 2012, ApJL, 746, L17

Wright, P. J., Hannah, I. G., Grefenstette, B. W., et al. 2017, ApJ, 844, 132

Zhang, Y., Musset, S., Glesener, L., Panesar, N. K., & Fleishman, G. D. 2023, ApJ, 943, 180